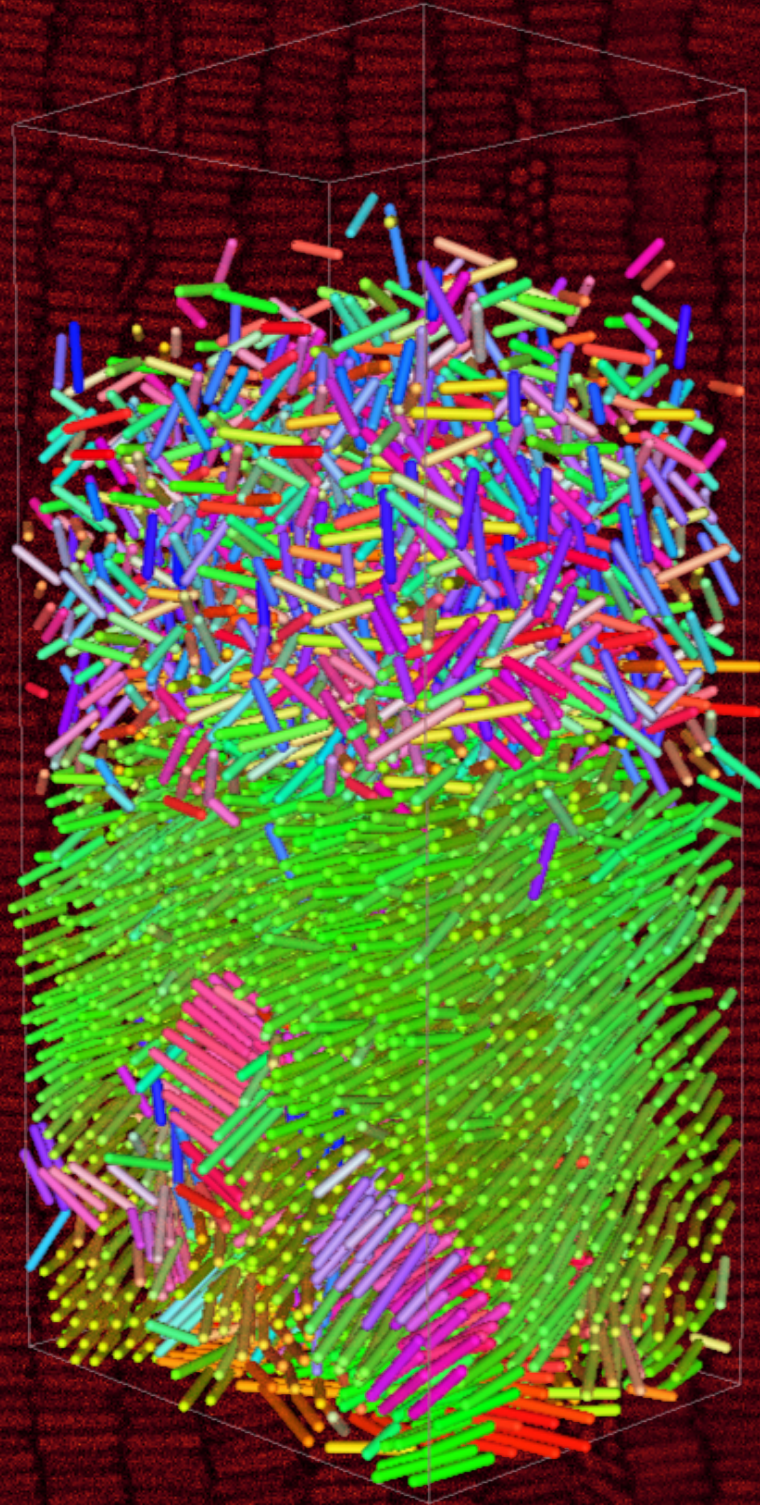# 3D Real Space Measurements on Colloidal Silica Rods in a Gravitational Field

Chris Kennedy

June 2014

3D Real Space Measurements on Colloidal Silica Rods in a Gravitational Field

Chris Kennedy

June 2014

Supervisors: Thijs Besseling, Arnout Imhof, Alfons van Blaaderen

Soft Condensed Matter
Debye Institute for Nanomaterials Science
Utrecht University

Contents

Contents

Abstract

The phase behaviour of rod-like colloidal particles with aspect ratios (L/D) of 4.7, 5.4 and 5.8 was studied in 3D real space using fluorescent silica particles and confocal microscopy. Full positional and orientational coordinates of an equilibrium sedimentation profile of $L/D = 5.4$ particles was obtained, allowing access to 3D density and order parameter profiles. From the density profile, the equation of state was calculated as well as an in-situ estimation of the gravitational length based on the barometric region. Fewer phases and lower coexistence densities were observed than were predicted by computer simulations of hard sphereocylinders at this aspect ratio. This is ascribed to the polydispersity ($\sim 10\%$ in length and diameter) of the system and the electrical double layer around the particles resulting in a change in their effective dimensions. Attempts were made to correct for these charge effects resulting in some qualitative agreement with simulations in terms of the observed phases and coexistence densities. Evidence was found for the result predicted by theory and simulations that the nematic order parameter profile trails the density profile when entering the isotropic phase, with good magnitude agreement. Preliminary results on $L/D = 5.8$ particles with lower polydispersity suggest that the nematic phase may be observable in this system.

1. Introduction

1.1. Colloidal Systems

Despite the almost complete absence of the word 'colloid' from the public consciousness, colloidal systems are ubiquitous throughout human civilization and the natural world beyond. The word describes a system in which 'little bits' of something are to be found in a continuous 'sea' of something else. The bits and the sea can be a combination of any two of: solid, liquid and gas (except both gas) which means that a wide array of different ensembles are encompassed by the term. For example, mist is made up of water droplets in air (liquid-in-gas), milk consists of oil globules in water (liquid-in-liquid) and many inks are small pigment particles in an aqueous medium (solid-in-liquid) [1]. The type relevant to this investigation is the final one mentioned, that of solid particles dispersed in a liquid phase. The size of the units of the dispersed phase sets the limit of what is termed colloidal, with the criterion that at least one dimension has a length approximately between $1\,\text{nm}$ and $1\,\text{μm}$ [2]. This definition is somewhat arbitrary however and the important meaning behind it is that colloidal particles are generally small enough to exhibit Brownian motion [3].

The usefulness of colloidal particles to humans may be roughly divided into two categories. The first is based on the application of the particles themselves. For example, white paints generally contain colloidal titania, with the size of the particles playing an important role in the ability of the paint to scatter light [4]. In the kitchen, colloids may be found in the particles of tomato pulp dispersed in a liquid medium to form tomato ketchup [5]. Closer to the cutting edge, the optical properties of some colloidal crystals may be used to create photonic crystals for novel waveguide applications [6].

The second use of colloids lies in the possibility to use them as a model condensed matter system and this is the one relevant to this research. It arises from the fact that the particles undergo Brownian motion and are hence able to sample a wide range of configurations. The upshot of this is that they can exhibit phase behaviour in the same way as atoms and molecules. The much larger size, and consequently slower dynamics, of colloidal particles means that their behaviour may be readily observed using optical microscopy [7].

The rod shaped particles used in this investigation are able to form liquid crystal phases, in direct analogue to assemblies of anisotropically shaped molecular moieties. They may therefore be used as an experimental test of important models of liquid crystalline systems, particularly the hard spherocylinder model. While most molecular liquid crystal systems are thermotropic (where the phase behaviour is controlled by temperature), colloidal systems are generally lyotropic, meaning that phase transitions are induced by changes in particle density (or equivalently, volume fraction). This means that a particle density gradient can exhibit all possible phases of the system along its length. Such a gradient may be achieved by allowing particles which have higher density than their surrounding medium to sediment against a confining wall at the bottom of their container under the force of gravity. This mechanism is at the heart of the present study.

1.2. Motivation and Aims of this Research

Kuijk et al. [8] studied equilibrium sediments of rod shaped silica particles and were able to construct a quantitative experimental phase diagram based on X-ray scattering methods. The

real space observations which were made during the same study were principally of a qualitative nature and it is the intention of the present research to build on the aforementioned investigation with quantitative measurements on sediments of colloidal silica rods in 3D real space. This is made possible by the recent development of a fitting method to obtain the positional and orientational coordinates of anisotropic particles imaged using confocal microscopy [9]. In this way, detailed information about the positions and orientations of single particles may be obtained. This information will be used to examine both the local environments of particles and look at more averaged information such as the density and nematic order parameter profiles. The results will be compared to the predictions made by theory and simulations on hard spherocylinder systems.

1.3. Organisation of this Thesis

In Chapter 2, the theoretical background of the project is discussed in terms of the internal and external forces governing the behaviour of colloidal particles. A brief introduction to selected liquid crystalline phases is given, along with the working principles of two important experimental techniques: the particle synthesis and confocal microscopy.

A description of the methods used to set up and extract information from the colloidal sediments is found in Chapter 3.

The results of the investigation are presented alongside a discussion of their implications in Chapter 4. Initially the emphasis is on the creation and optimisation of the system and laterally the focus moves to measurements and observations of the sedimentation profiles.

The 5th and final chapter contains the conclusions drawn from the investigation and suggested areas for future research.

2. Theory

2.1. Interactions of Silica Colloids

The interactions of colloidal particles are complex and involve a wide array of physical and chemical phenomena which have given rise to a vast literature of theoretical and experimental study. Volumes have been compiled on the behaviour of colloidal silica alone, partly due to this general complexity and partly to its many applications [10]. This report is concerned with the use of silica particles as a model experimental system, not with an application of the particles themselves in mind, so this section will be limited to the most relevant fundamental interactions.

2.1.1. The Charged Surface

A negative surface charge emerges on a silica surface in contact with a polar solvent (provided that the solvent is not extremely acidic) due to the dissociation of terminal silanol groups: $-\mathrm{SiOH} \rightleftharpoons -\mathrm{SiO}^- + \mathrm{H}^+$. What is known as an electrical double layer is then formed at the surface. This is described as follows in a theory developed by Otto Stern as a combination of the Helmholtz and Gouy-Chapman models [11]. The first of the two eponymous layers (of ions) is that of hydrated cations electrostatically 'attached' at their distance of closest approach to the surface (the Outer Helmholtz Plane, OHP). The second layer is a diffuse atmosphere which contains an excess of cations such that the surface charge is completely balanced by the two layers. The shape of the potential variation may be seen from Figure 2.1.

The potential is assumed to rise linearly from the surface potential, ψ_S, to the OHP potential, ψ_d, after which point the potential decays exponentially (Debye-Huckel approximation) towards 0 infinitely far into the bulk solution. The size of the double layer, and distance at which the surface charge is fully screened, is characterised by κ, the exponential decay constant. The Debye length, κ^{-1}, is the distance at which the potential has fallen to ψ_S/e, where e is $\exp(1)$ [12]:

$$\frac{1}{\kappa} = \left(\frac{\epsilon_r \epsilon_0 kT}{2 c_i e_q^2} \right)^{\frac{1}{2}} \tag{2.1}$$

ϵ_r and ϵ_0 are the (relative) permittivity of the medium and free space, kT is the thermal energy characterised by Boltzmann's constant, k, and the absolute temperature, T. The ionic strength of the continuous medium is denoted c_i and e_q is in this case the electronic charge. In practice, the ζ potential (defined as the potential at the slipping plane) is used in place of ψ_S due to its experimental accessibility [13].

The total interaction energy is described by a theory developed by Deryaguin and Landau and Verwey and Overbeek (DLVO theory). The basis of this theory is that the interaction energy between two particles is the sum of contributions of the attractive London dispersion force (the most relevant of the van der Waals forces in this case) and repulsive interaction of the two double layers. London dispersion forces are short ranged and their strength is characterised by the Hamaker constant, A, which depends on the relative polarisability of the particle and solvent media. In this case of two particles of the same material interacting via a solvent, the force is always attractive and the Hamaker constant is calculated using Equation 2.2 [14]. ϵ_c and ϵ_s are the dielectric constants of the colloid material (silica) and solvent respectively, $h\nu_e$ is the energy of a photon at the main UV electronic absorption frequency and n_c and n_s are the refractive indices in the visible region.
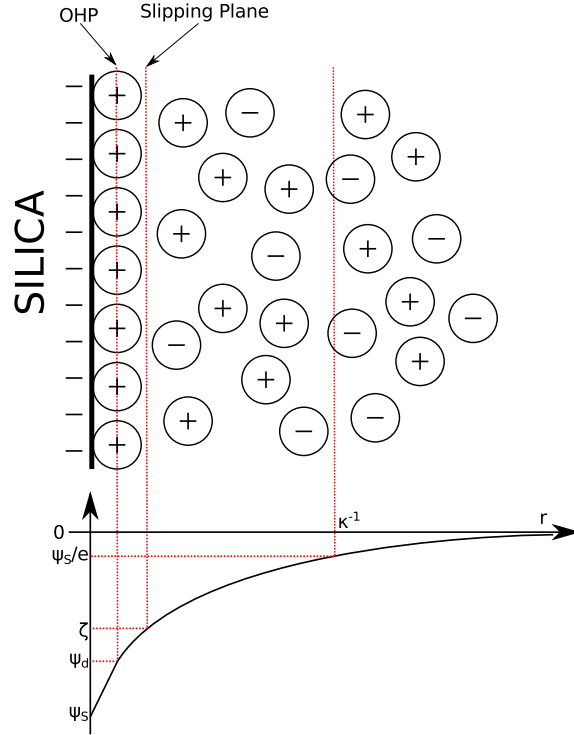
2. Theory

Figure 2.1.: Schematic representation of the double layer showing the corresponding potentials on bottom axes. The outer Helmholtz plane (OHP) is through the centres of the ions in the Stern layer (attached to surface) and the diffuse layer extends out to a distance $r = \kappa^{-1}$ from the surface [11].

$$A = \frac{3}{4}kT\left(\frac{\epsilon_c - \epsilon_s}{\epsilon_c + \epsilon_s}\right)^2 + \frac{3h\nu_e}{16\sqrt{2}}\frac{(n_c^2 - n_s^2)^2}{(n_c^2 + n_s^2)^{\frac{3}{2}}} \tag{2.2}$$

The consequence of the dependence on the dielectric constant and refractive index in Equation 2.2 is that when the refractive indices of the colloid and solvent are matched, the Hamaker constant is reduced to such a degree that the dispersion interaction energy is much less than kT. Refractive index matching also drastically improves the quality of fluorescence microscopy images and all suspensions studied in this investigation were prepared such that $n_s = n_c$. Therefore the effect of van der Waals attractions may be neglected.

The other contributor to the pair potential in DLVO theory is the double layer repulsion. When two particles approach such that their diffuse ion clouds begin to overlap, it is not possible for the potential of either to decay to zero as it does in Figure 2.1. Instead, there is a non-zero potential at the midpoint between the two particles which results in repulsion. The electrostatic energy of repulsion, $U(r)$, depends on the inverse Debye length, κ, and interparticle distance, r:

$$U(r) \propto \frac{\exp(-\kappa r)}{r}. \tag{2.3}$$

Therefore, in an index matched system such as that studied here, the interparticle potentials are almost purely repulsive with their 'softness' characterised by the Debye length (a low Debye length corresponds to interactions similar to hard core repulsion where two particles can approach until their surfaces touch but may not overlap). However, the colloids in this investigation will not disperse themselves uniformly throughout their medium as might be suggested by the preceding discussion. They will be forced to approach each other at distances on the order of their Debye length by the external force of gravity, as discussed in the following section.

2.2. Colloidal Sedimentation

2.2.1. General Case

A dilute suspension of colloidal particles in the ideal gas limit (dilute enough to be non interacting) acted on by a uniform gravitational force equilibrates to an exponentially decaying density profile in the direction parallel to gravity, z. This behaviour was experimentally proven by Perrin and is described by Equation 2.4.

$$\rho(z) = \rho(0) exp\left(-\frac{z}{l_g}\right) \tag{2.4}$$

$\rho(z)$ is the particle number density at height z and l_g is the gravitational length, $l_g = kT/mg$, where mg is the buoyant weight of a single particle. The buoyant mass, m, is obtained from Archimedes' principle which states that the buoyant force is equal to the weight of displaced fluid by a particle with volume V_p: $m = \Delta\rho_m V_p$. $\Delta\rho_m$ is the density difference between colloid and solvent. In the case that the solvent material is denser than that of the colloid, l_g is negative and the particles sediment against gravity but for silica particles in most conventional solvents, l_g is positive and the particles sediment towards the Earth.

For higher concentrations, when interparticle interactions may no longer be neglected, the sedimentation system may be considered in terms of a macroscopic equilibrium, as follows. Equilibrium is reached when the gravitational pressure distribution, $-mg\rho(z)$, is balanced by the osmotic pressure gradient:

$$\frac{d\Pi(z)}{dz} = -mg\rho(z) \tag{2.5}$$

where $\Pi(z)$ is the height dependent osmotic pressure. Integration of a known sedimentation profile (such as that obtained from an experimental measurement) from z to the top of the sample at h allows extraction of the osmotic pressure as a function of height:

$$\Pi(z) = -mg \int_z^h \rho(z) dz \tag{2.6}$$

At equilibrium, $\rho(h) = \rho(\infty) = 0$ so Equation 2.6 is equivalent to the statement that the osmotic pressure at any height in the sediment is simply the weight per unit area of all the particles above it [15]. z can be eliminated between the density profile and osmotic pressure distribution, yielding the equation of state $\Pi(\rho)$.

If the equation of state is known beforehand, the density profile may be predicted by assuming isothermal conditions and introducing the osmotic compressibility $\chi_T = (\partial\Pi/\partial\rho)_T^{-1}$:

$$\frac{d\rho(z)}{dz} = -\frac{\chi_T(z)}{l_g}\rho(z) \tag{2.7}$$

The macroscopic nature of this analysis is not without consequence. The implicit assumption is made that the density profile is constant over macroscopic length scales, or at least over length scales larger than the interaction distances of the particles. This is not the case for dense sediments of colloidal particles against a flat wall, in which case layering of particles is expected, and hence oscillating density profiles. In a Density Functional Theory (DFT) treatment of sedimentation equilibrium the macroscopic results are recovered only if a Local Density Approximation (LDA) is applied. Corrections may be made to the LDA to predict the layering behaviour at low z but these are not analytically solvable [16]. In order to compare experimental density profiles (or those obtained from computer simulations) with the macroscopic/LDA case, coarse graining may be applied by convolution with a resolution function (such as a normalised top hat of width a few particle diameters).

2.2.2. Rod-Shaped Particles

The sedimentation equilibrium described above is applicable to rods as much as spheres or any other shaped particle but the dynamics of sedimentation in dilute suspension are more specific to the form of the particle. The sedimentation velocity of a lone colloidal particle in a fluid is given by the Svedberg equation [17]:

$$v_{sed} = \frac{V_p D_t g \Delta \rho_m}{kT}. \tag{2.8}$$

As it stands, Equation 2.8 is still a general one because the specificity is hidden under the veil of the (orientationally averaged) translational diffusion coefficient, D_t. The calculation of the diffusion coefficient of a finite rod shaped particle is not trivial due to end effects but the form is that shown in the first of Equations 2.9 (both of which apply only to cylinders without spherical ends, so are used as an approximation). The rotational diffusion coefficient, D_r, may be calculated in a similar way [18, 19].

$$D_t = \frac{kT(\ln\left(\frac{L}{D}\right) + \nu)}{3\pi\eta_0 L} \qquad \text{and} \qquad D_r = \frac{3kT(\ln\left(\frac{L}{D}\right) + \delta_\perp)}{\pi\eta_0 L^3} \tag{2.9}$$

In these expressions, L is the total length of the rod with diameter D, η_0 is the solvent viscosity and ν, $\delta_\perp$ are the end corrections. These naturally depend on the aspect ratio of the particles and may be estimated using Equations 2.10 and 2.11 [20, 21].

$$\nu = 0.312 + 0.565\frac{D}{L} - 0.100\left(\frac{D}{L}\right)^2 \tag{2.10}$$

$$\delta_\perp = -0.662 + 0.917\frac{D}{L} - 0.050\left(\frac{D}{L}\right)^2 \tag{2.11}$$

The final requirement for the calculation of the sedimentation velocity is the volume of the particle. This may be calculated by assuming a spherocylindrical shape:

$$V_p = \frac{1}{4}\pi D^2\left(L - \frac{D}{3}\right). \tag{2.12}$$

The particles used in this investigation are neither perfectly spherocylindrical or perfectly cylindrical, but somewhere in between as may be seen from Figure 4.1 but this treatment is sufficient to obtain estimates of the sedimentation velocities.

2.3. Phase Behaviour of Rod-Shaped Colloids

In contrast to a uniform spherical particle, different orientations of an anisotropic particle are distinct. This means that in an assembly of such particles, not only the relative positions of the particles determine the phase behaviour, but also the relative orientations. Anisotropic particles therefore exhibit additional phases known as liquid crystals which are characterised by different degrees of orientational and translational order. As their name suggests, these phases have properties intermediate between those of the liquid and the crystal and are found at similarly intermediate points in the phase diagram. Brownian motion allows colloidal particles to sample many configurations and reach thermodynamic equilibrium. Figure 2.2 illustrates possible phases of a system of spherocylinders. The lowest density phase is the isotropic, which exhibits no orientational order. The higher density nematic phase is characterised by orientational order such that the particles have a nonzero average orientation. The smectic phases show a greater degree of particle alignment and also a periodic arrangement in space, forming layers in one (known as smectic-A) or two dimensions (smectic-B). Full alignment is found in the columnar
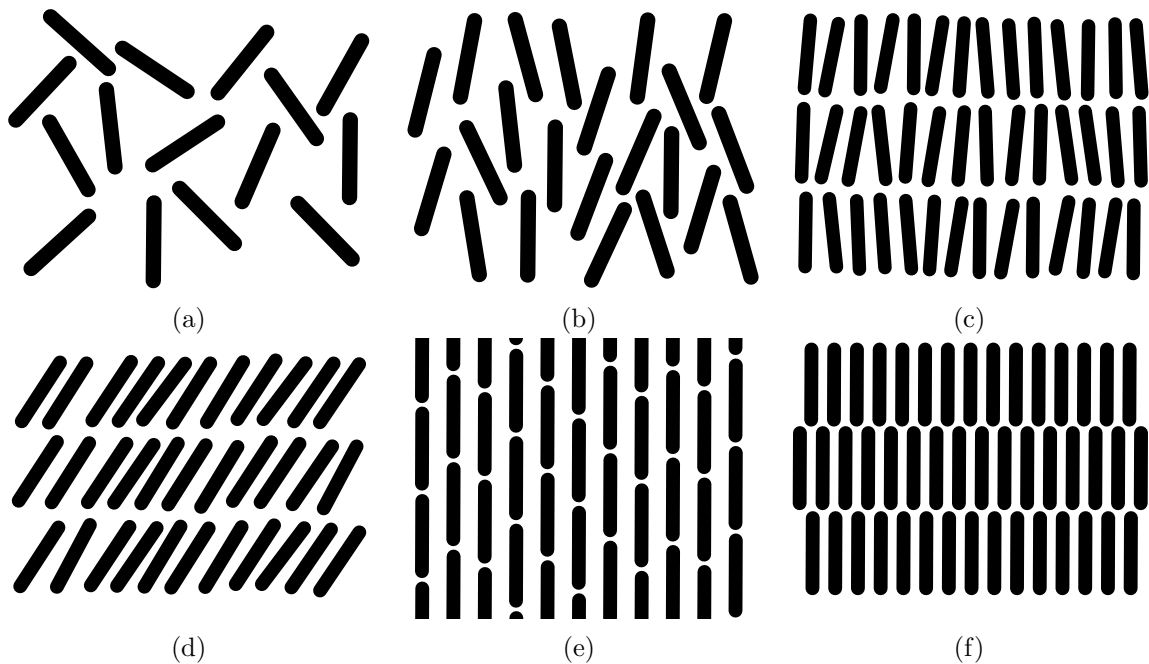
Figure 2.2.: Liquid Crystal Phases: (a) Isotropic: No ordering. (b) Nematic: Orientational but not translational order. (c) Smectic-A/B: Orientational order and translational order in one (A) or two (B) dimensions. In the smectic-B phase, the particles are arranged hexagonally within the layers. (d) Smectic-C: Orientational order and translational order in one dimension. In this case the director (average orientation) is not perpendicular to the layers but at an angle. (e) Columnar: Orientational order (full alignment) and translational order in two dimensions. Particles are hexagonally arranged but not layered along their long axes. (f) Crystal: Full orientational and translational order in three dimensions.

and crystal phases with the difference being that columnar particles have translational order in two dimensions (hexagonal but without the layering found in the smectic-B) and crystalline particles are periodically arranged in three dimensions.

2.3.1. Hard Spherocylinders (HSC)

As in any area of study, the simplest model is a good one to start with and for this reason the system of rigid spherocylinders interacting purely through hard core repulsion is the most studied both in theory and computer simulations. Onsager pioneered this area in 1949 with his studies of rigid rods with infinite aspect ratio [22]. He showed that the isotropic-nematic transition is driven by the gain in entropy associated with the decreased excluded volume, relative to the isotropic phase, at high density. More realistic systems of particles with finite aspect ratio do not have exact solutions as the Onsager model does but computer simulations are able to provide insight and predictions. In the late eighties, evidence for both the nematic and smectic phases was found using Monte-Carlo simulations on L_{cy}/D=5 systems (where L_{cy} refers to the cylinder length, commonly used to define the particles size in simulations) [23, 24]. Simulations have since allowed the full phase diagram to be predicted as a function of aspect ratio, as shown in figure 2.3 [25]. It may be seen that the phase behaviour becomes richer at higher aspect ratio with the onset of the smectic (A) and nematic phases at L/D values of 4.1 and 4.7 respectively.
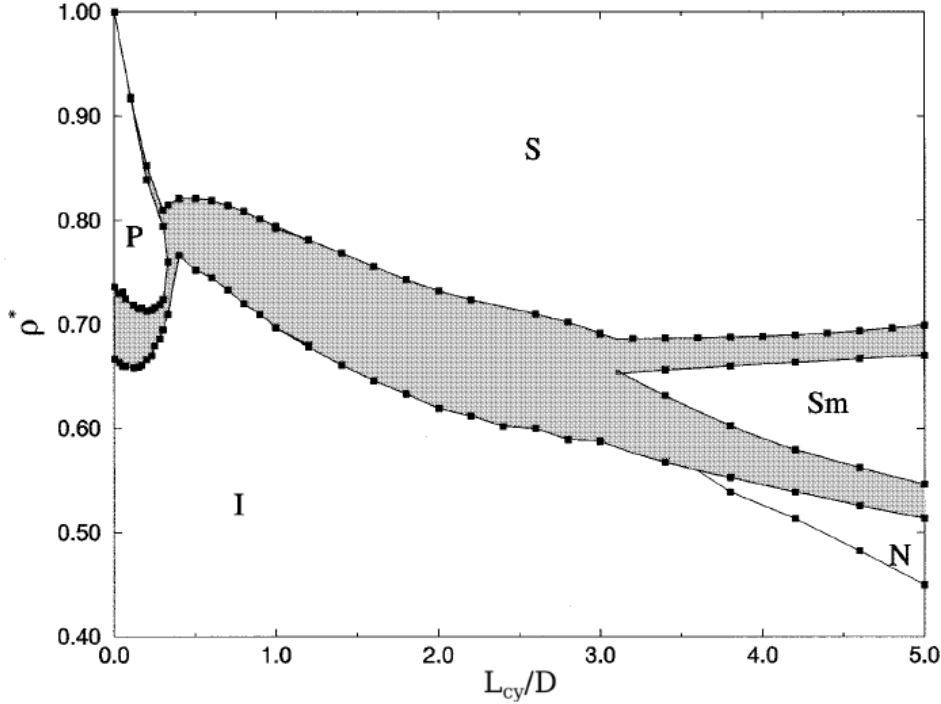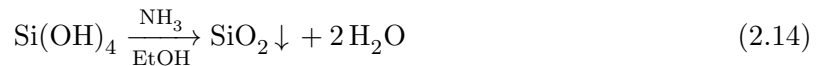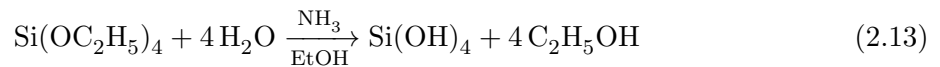
Figure 2.3.: HSC phase diagram predicted by simulations [25]. ρ^* is the density relative to close packing and L_{cy}/D is the aspect ratio of the particles. The letters identify the equilibrium phases: (P) Plastic Crystal, (S) ABC stacked crystal, (Sm) Smectic A, (N) Nematic and (I) Isotropic. Grey areas indicate coexistence. When working with computer simulations, the aspect ratio is characterised by the cylinder length whereas in experiments L refers to the full length including the spherical ends. In this report, L and L_{cy} will denote the full and cylinder lengths respectively. Aspect ratios translate simply: $L/D = L_{cy}/D + 1$.

2.4. Synthesis Mechanism of Rod-Shaped Silica Particles

The synthesis mechanism is described in detail in Reference 26 but will be briefly outlined here. The base catalysed reaction of tetraethoxysilane (TEOS) to silicon dioxide has been used for many years in the synthesis of colloidal silica spheres [27, 28]:

$$Si(OC_2H_5)_4 + 4\,H_2O \xrightarrow[\text{EtOH}]{\text{NH}_3} Si(OH)_4 + 4\,C_2H_5OH \tag{2.13}$$

$$Si(OH)_4 \xrightarrow[\text{EtOH}]{\text{NH}_3} SiO_2\downarrow + 2\,H_2O \tag{2.14}$$

For spherical particles, this hydrolysis/condensation reaction is carried out in ethanol. To synthesise anisotropic particles, the same reaction is used under different conditions, resulting in a different growth mechanism.

An emulsion of water in pentanol may be formed in the stabilising presence of the polymer polyvinylpyrrolidone (PVP) and sodium citrate. With ammonia and ethanol also present, the addition of TEOS to this emulsion begins the growth of rod shaped particles. Reaction 2.13 results in a hydrophilic species which migrates into the water droplets. The silica nucleus is found to form on the surface of a water droplet and since the condensation precursor is inside the droplet only, the silica condenses onto only one side of the nucleus. This process continues with silica always added from only one side, resulting in a rod shaped particle. Once the supply of TEOS is exhausted, the drop remains on the end of the rod until it is washed away after the

reaction. The 'front' end of the rod is rounded and the 'back' end (where the water droplet was attached) is flat: the particles are bullet shaped.

2.5. Confocal Microscopy

As mentioned in Chapter 1, colloidal particles may be observed using optical microscopy. The technique of confocal microscopy is particularly well suited to the study of colloidal systems.

When a point light source is imaged in 3D by a (diffraction limited) microscope, what is observed is the point spread function (PSF) of the imaging system. This is the three dimensional equivalent of the Airy disk. In a conventional (wide field) fluorescence microscope, the PSF exhibits significant intensity in a cone shape above and below the point [29]. A bulk fluorescent object is excited all at once and may be considered as a series of point light sources, each of which contributes a PSF to the image. The result of the axial extent of the PSF is that light from planes which are not in focus contribute significantly to the image, causing blurring. This limits the technique to observation of very thin fluorescent samples.

The confocal microscope modifies the PSF using a pinhole in the confocal plane [30]. The pinhole only allows light rays originating from the focal plane to reach the detector, so the PSF is significantly diminished in the axial direction. A smaller pinhole allows finer optical sectioning but also rejects more light, decreasing the signal to noise ratio. The pinhole size is therefore a compromise and is generally around one Airy unit (after magnification), with the optimal size depending on the system and required images. By matching the refractive index of the immersion fluid, solvent and particles, light scattering may be minimised. This means that sharp images, with a low depth of field, may be captured deep within a fluorescent object or assembly.

The second difference in the confocal arrangement is the illumination of one point at a time [31]. This provides an increase in the lateral resolution of the microscope which improves with diminishing field of view [29]. The size of the effective field of view is returned to a useful one by scanning the sample using a laser (other methods have also been used to achieve this scanning). A 3D image volume is built up by rapidly scanning the laser across the field of view to build up a 2D picture, one pixel at a time. The sample stage is then moved slightly along z and another 2D image captured, and so on.

3. Methods

3.1. Particle Synthesis

The silica rod synthesis used in this project is based on the core-shell method developed by Kuijk et al. [26]. This was scaled up in order to yield quantities of as synthesised rods of approximately $1.4\,g$. Modifications were made to the water and ammonia concentrations, as well as the reaction temperature, to increase the aspect ratio of the resulting particles.

3.1.1. Core Particles

In all syntheses, $80\,g$ of polyvinylpyrrolidone (PVP, Sigma Aldrich, avg. mol. wt. $40\,kg$) was dissolved in $800\,mL$ of 1-pentanol (Sigma Aldrich, $\geq 99\%$) by shaking and sonication in a $1\,L$ reaction bottle. After temperature equilibration, $80\,mL$ of ethanol (absolute, Baker) was added along with deionised water (Millipore System, quantities in Table 4.1) and $8\,mL$ of $0.18\,M$ sodium citrate (tribasic dihydrate, Sigma Aldrich, $\geq 99\%$). The reaction bottle was shaken by hand to create a turbid emulsion. Ammonium hydroxide solution (ammonia, Sigma Aldrich, 25% wt.) and tetraethyl orthosilicate (TEOS, Sigma Aldrich, 98%) were then added respectively in the quantities shown in Table 4.1. The reaction bottle was sealed and briefly shaken to fully mix the reactants before being left undisturbed for 3 days.

The particles were separated from the reaction mixture by centrifugation ($1500\,g$/2 hours, where g is $9.81\,ms^{-2}$) followed by washing twice with ethanol (100%, Interchema) and twice with deionised water before being washed once more with, and dispersed in, ethanol.

The synthesis yielded particles with polydispersity in both length and diameter of around 20%. Therefore, small particles were removed by centrifuging (e.g. $200\,g$/10 minutes) and removing the top of the turbid supernatant. Large particles and aggregates were removed by allowing $40\,mL$ of dispersion to sediment for several hours and then recovering approximately $3\,mL$ from the top of the vial. This was repeated until around $1\,g$ of silica had been recovered.

3.1.2. Preparation of Particles for Confocal Imaging

For confocal microscopy imaging, the rods were coated with a fluorescently labelled silica shell using the method described in Reference 32. $25\,mg$ (excess) fluorescein isothiocyanate (FITC, isomer I, $\geq 90\%$, Sigma Aldrich) was dissolved in $5\,mL$ of absolute ethanol to which $35\,\mu L$ of the silane coupling agent, (3-aminopropyl)triethoxysilane (APS, $\geq 98\%$, Sigma Aldrich) was added. This mixture was then covered to prevent light entering and left undisturbed to react overnight.

The coating was carried out by first dispersing the rod cores (approximately $1\,g$ of silica) in $300\,mL$ of ethanol and adding $10\,mL$ of both deionised water and ammonia under gentle magnetic stirring. 0.5-$1\,mL$ of TEOS was then added, quickly followed by the dye mixture. This was left stirring lightly overnight. The particles were separated from the reaction mixture by centrifugation ($600\,g$/30 minutes) and washed 3 times with ethanol.

In order to separate the fluorescent signals of the particles to such a degree that single particles could be located in dense sediment (Section 3.2.4), non fluorescent Stöber silica shells were grown to thicknesses of around $130\,nm$ in about three steps using well established methods [32]. This procedure is very similar to that of the fluorescent coating described previously but with the omission of FITC and APS. After the final coating, the particles were washed in water

3. Methods

Name	Constituents (Mass Ratio)
GW	Glycerol:Water (85:15)
SGW	Glycerol:Water (85:15), 4.5×10^{-4}molkg^{-1} LiCl
DW	DMSO:Water (91:9)
GDW	Glycerol:DMSO:Water (47:44:9)

Table 3.1.: Index-matching solvent mixtures used in this investigation. Discussion of the differences is in Section 4.2.2. DMSO refers to dimethyl sulfoxide.
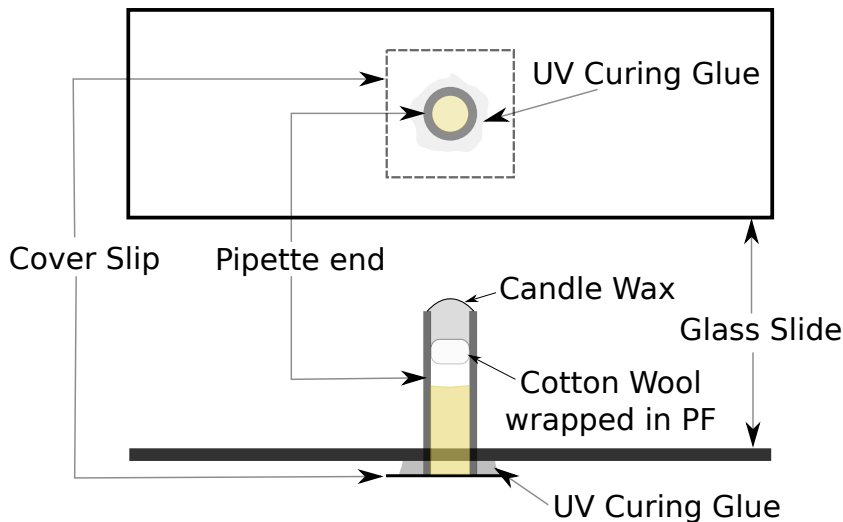

Figure 3.1.: Top and side views of the principal cell used in this investigation. PF refers to Parafilm. If the suspension is incompatible with UV curing glue, the bottom of the cell can also be sealed with candle wax.

and any floating debris removed by overflowing (thought to be PTFE scratched off the stirrer bar during coating).

The particles were imaged with transmission electron microscopy (TEM, FEI Tecnai 10 or 12) after synthesis and each shell coating to determine their dimensions. At least 100 particle lengths and diameters were measured in each case to provide reliable average dimensions and polydispersity values.

With extensive centrifugation/sedimentation, the polydispersities of the final rods were reduced to around 10% in both dimensions. These particles were then dispersed in an index matching solvent with $n_D^{25} = 1.45$ (see Table 3.1) for confocal imaging.

3.2. Microscopy and Image Processing

3.2.1. Cell Preparation

Except where indicated otherwise, the cells used in this investigation were of the form shown in Figure 3.1. This is constructed by cutting the end (where the bulb would attach) off a glass Pasteur Pipette (WU Mainz, short size, cross sectional area $22.1\,\mathrm{mm}^2$), sanding the bottom flat and gluing it to a microscope cover-glass appropriate for the intended objective lens. A hole is drilled in a glass slide and the pipette end fed through and glued at the bottom so that the cell may be held in a conventional microscope stage. The column is then filled with index matched suspension and plugged at the top with cotton wool wrapped in Parafilm and finally sealed with candle wax. This cell can be filled with very dilute suspension (volume fraction, ϕ, on the order of 10^{-4}) which will eventually form a concentrated sediment at the bottom. It is known that

DMSO containing solvents are not compatible with UV curing glue so in this case the bottom of the cell was sealed with candle wax [33].

3.2.2. Application of an Electric Field to the Sediment

In order to investigate the effect of external alignment of the particles during sedimentation, an electric field was applied to a sedimenting system. This was achieved using the cell described in Appendix B which is very similar to the normal cell but with the addition of two rails of thermocouple wire (Goodfellow Metals, T2 Alloy, 50 μm diameter, centres approximately 575 μm apart) across the bottom of the column.

An isotropic suspension of L/D=4.7 particles in GDW solvent was sealed in the cell and allowed to sediment for 6 days. A 1 MHz, 19 mV μm^{-1} ($V_{rms} = 10.9$ V measured with oscilloscope) electric field was then applied for approximately 40 minutes, inducing alignment of the particles along the field direction. Such a field was chosen so as not to move the particles, but simply align them, and not polarise the double layer. The theoretical basis for the alignment of anisotropic particles in an electric field is described elsewhere [21]. The particles were then left undisturbed for 59 days before imaging the sedimentation profile.

3.2.3. Confocal Microscopy

Confocal microscopy images were recorded with a Leica SP8 with one of the following (Leica) immersion lenses: 100×/1.4 (oil) and 100×/1.35 (glycerol). These lenses were found to be the most suitable after the testing described later in this section. Image stacks of approximately 25×25×100 μm were recorded using a 488 nm excitation laser line selected from a white light laser and a 12 kHz resonant scanner and hybrid detector. As it was desired to deconvolve the images (see Section 3.2.5), a high sampling rate was required with corresponding voxel dimensions of approximately 50×50×80 nm. As there are limits to how many pixels may be scanned across in the x-y plane, low pixel dimensions lead to a small field of view. To counter this, many image volumes may be captured in adjacent (and slightly overlapping) regions ('tile scanning'). These images are then merged together to create an overview image volume. The merging of tiles is effective when capturing 2D images but with 3D data, the time between the imaging of each volume is relatively long, particularly between two tiles adjacent in the y direction. This means that except in a stationary sample, merging of image volumes results in motion blur along the overlap regions.

In addition to high resolution, imaging of sediments from below requires a long working distance such that the whole sediment can be imaged. In this investigation, three lenses were tested, shown in Table 3.2. Each objective is manufactured for use with a certain cover-glass material and thickness as both of these affect the path of light. The lenses were coupled with the cover-glasses appropriate to them (Table 3.2) and a thinner, 170 μm (#1.5), one was also investigated for the 100×/glyc lens. Capillaries were not used as cells due to their poor optical quality [30]. Test sediments were prepared by adding 350 μL of suspension (L/D=4.7, see Table 4.2, $\phi \approx 0.2\%$) to three different cells and leaving them undisturbed for 4 days before imaging. The particles were dispersed in GDW solvent and the imaging parameters are shown in Table 3.3. Both glycerol immersion lenses were equipped with correction collars which were adjusted before imaging. This may be done with the microscope in reflection mode [34] but it was found to be more convenient to simply search for highest clarity and intensity in fluorescent x-z images. x-y images should not be used for correction collar setting as adjustment causes shift of the focus along z so features move in and out of focus. This makes it difficult to see the intensity gain when the collar is correctly set.

Lens	Cover-glass	Immersion n	Glass n
$100\times$/oil	#1.5: $170\,\mu$m Borosilicate	$n_e^{23} = 1.5180$	$n_e = 1.5255$
$63\times$/glyc	#1.5: $170\,\mu$m Borosilicate	$n_D^{21} = 1.45$	$n_e = 1.5255$
$100\times$/glyc	#2: $200\,\mu$m Fused Quartz	$n_D^{21} = 1.45$	$n_D^{20} = 1.4584$ [35]

Table 3.2.: Intended cover-glass/objective lens combinations. All lenses and immersion oil are manufactured by Leica. Borosilicate cover-glasses were obtained from Menzel-Gläser and quartz ones from UQG Optics. A GW solvent mixture with measured refractive index was used as the glycerol immersion. The immersion oil and borosilicate refractive indices are as stated by the manufacturers.

Parameter	Value	Parameter	Value
Image Dimensions	$25.8\times13.3\times100(\pm2)\mu$m	Image Size	$512\times265\times1192\,$px
Laser power	9% (of 70%)	Voxel dimensions	$50.4\times50.4\times80\,$nm
Gain	20	Averaging	5 Lines
Pinhole Radius	0.8 Airy Units	Imaging Time	$83\,$s
Frame Rate	15.9/s	Scanning	$12\,$kHz Bidirectional

Table 3.3.: Imaging parameters for all lens tests.

3.2.4. Extraction of Positional and Orientational Coordinates

The feature fitting algorithm used in this investigation was that developed by Besseling and Hermes which will be briefly discussed in this section alongside a demonstration on an experimental image stack. The motivation for the development of this novel method was the desire to fit the positions and orientations of rod-shaped particles in concentrated phases where there is significant overlap of the fluorescent signals of adjacent particles. An extensive discussion of the procedure is given in Reference 9. In this research, image volumes were deconvolved before fitting as discussed in Section 3.2.5.

The first stage of the fitting routine involves some preliminary image processing. The image volume is read in as a series of 8 or 16-bit images and a normalised greyscale value assigned to each element in the volume (voxel). Due to the imaging technique, the z sampling rate is usually about half of the x-y sampling, resulting in a cuboidal voxel. In order to avoid effects of this anisotropy later in the fitting procedure, the image may be scaled up in the z direction using bicubic interpolation to obtain cubic voxels. In this investigation it was found that the particle fitting was more effective without scaling the images but simply scaling the resulting particle coordinates along z after completion of the fitting steps. The z component of the rod lengths was similarly scaled.

The next step is to apply a Gaussian blur to the image to lessen the effects of noise. The width of the blur is adjusted manually after visual inspection as the optimal value is specific to the image. A blur diameter of 3 pixels (or about a quarter of the particle fluorescent diameter) in x,y and 1.5 in z was typical in this investigation. An absolute background value is subtracted from each voxel to leave each particle with a black background.

The next stage in the method is the search for particle backbones, i.e. the straight line of bright pixels which should follow the middle of a uniformly dyed rod. In the case of particles with fluorescent shells, as utilised in this investigation, the Gaussian blur ensures that the brightest line is along the middle of the particle. In the example shown in Figure 3.2, this is of more importance than noise reduction since noise is already removed by the deconvolution (compare the third particle on the right before (b) and after (d) the blur). The backbone search is carried out by examining all the voxels brighter than a certain threshold value which is adjustable depending on the intensities in the image. Backbone voxels should be either local maxima or only have brighter pixels on one or two sides, in which case the three voxels must

be collinear. Collinearity is tested by fitting a straight line to the voxels and checking that the sum of the squared residuals is less than a certain cut-off value (a measure of the goodness of the line fit).

Due to the changing phases and decrease in signal intensity with increasing z height in confocal image volumes obtained using a mismatched (oil immersion) objective, in some cases it was useful to apply different fitting parameters (threshold value, blur radius etc.) at the top and bottom. The values used at intermediate heights were simply a linear scaling of these two values. The optimal relationship between the top and bottom parameters was found to depend on the images with the exception of the threshold value. Setting this very high in the region of the bright particles lying on the glass slide can speed up the computation in large image volumes. In this research, a value of 0.9 (fraction of the normalised intensity) at the bottom of the volume, scaled towards 0.5 at the top was found to be appropriate in many cases.

Once the backbone voxels have been found, those that lie close to each other are grouped with their neighbours resulting in a separate cluster of voxels for each particle (Figure 3.2c). A least squares fitting routine is applied to fit a new straight line to the pixels belonging to each rod. At this point, an estimate of the position, length and orientation of each rod are available but must be further refined to eliminate pixel bias which results from each rod having relatively few backbone voxels. Therefore the next stage is to apply another fitting procedure around these approximate locations.

Despite the large increase in visual appeal resulting from the Gaussian blur, there is also an inherent loss of resolution so the final fitting stage is applied to the unfiltered image. The position of each particle is taken as the centre of mass of the voxels (weighted with their intensity) close to (within one particle radius) the backbone of the previous fit. Least squares fitting is applied to these voxels to obtain the orientation vector of the particle. The length of the rod is determined by locating its end points. This is done by (manually) setting a cutoff value in the smoothed and normalised intensity histogram (values between 0.6 and 0.7 worked well) along the length of each rod. The ends of the rod are determined by fitting a straight line across the voxel where the intensity histogram falls below this cutoff using two voxels on either side of it. In this way, sub pixel accuracy may be achieved.

After the fitting is complete, filtering of particles which appear to overlap (i.e. have been fitted twice) are removed along with those which have very little intensity or are very short. The fit is checked visually by overlaying the found particles over the image (Figure 3.2d) and the input parameters adjusted until almost all of the particles have been correctly identified. Particles spanning the box edges have spurious locations and are removed by decreasing the x-y box size after inspection of the density profile in these directions (peaks are observed therein due to many centres of mass aligned along box edges). A full set of positional and orientational coordinates is available for each rod with reference to a box containing the imaged volume. The box is scaled along the z direction (along with all contained coordinates) to account for voxel aspect ratio (if the images were not scaled), refractive index mismatch between immersion fluid and the suspension (for oil lens only, 5%) and a calibration error in the microscope (3%) [36]. Besseling et al. [9] tested the uncertainty introduced by the fitting method for well separated particles, and found values of 0.05 particle diameters (as seen by the microscope, which in this test was approximately 300 nm) in position and 0.07 rad in orientation (4.01°). As the fluorescent signals are not in general well separated in this investigation, these uncertainty estimates will underestimate the true uncertainty in the results.

3.2.5. Deconvolution

As the point spread function can be measured or calculated for a particular microscope system, it is possible to deconvolve each point in the image with the appropriate PSF and obtain images with higher resolution. The additional information is provided by the incorporation of knowledge of the imaging system into the images during the deconvolution process [37]. The limiting
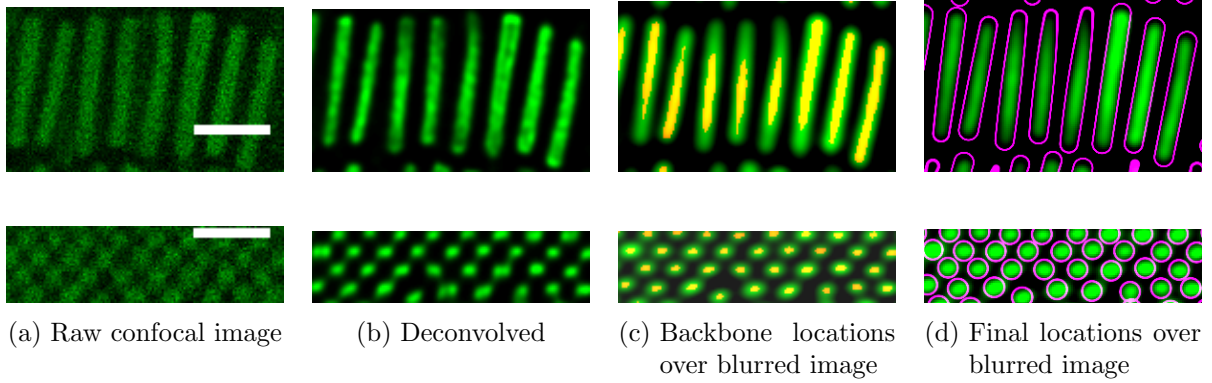
3. Methods

(a) Raw confocal image   (b) Deconvolved   (c) Backbone locations over blurred image   (d) Final locations over blurred image

Figure 3.2.: Series of images in x-y (top) and x-z (bottom, not scaled to cubic voxel) directions showing feature fitting steps on rods in a smectic phase. Scale bars are 2µm in x,y directions. z scale not shown but may be conveyed by the z height of bottom images: 3.16µm. Rods which are not exactly in the plane of this slice appear to have backbones which do not span the length of the rod in (c) and shapes deviating form a spherocylinder in (d). When visualised in 3D, these rods are found to be correctly identified.

requirement of this procedure is that the sampling rate is sufficient to provide information on the scale of the PSF. If several PSFs are captured within one voxel, information is irrecoverably lost and the deconvolution procedure is ineffective. For the microscope used in this investigation, a voxel size of $50\times50\times80$ nm was chosen such that images could be deconvolved to a significant extent. This represents almost ideal sampling in xy and oversampling in z. If the image data is oversampled, the effective dynamic range of the images can be increased by the deconvolution procedure [37]. The increased sampling rate is at the expense of the volume of the field of view (or the rapidity of the imaging) so ideally, particle fitting would sometimes be carried out using undersampled images. In practice it was found that for the specific particles in this investigation, deconvolution was generally necessary to locate all of the particles accurately.

Deconvolutions were carried out with Huygens Professional using the Classic Maximum Likelihood Estimation algorithm [38]. It is known that the PSF in confocal microscopy depends on the imaging depth due to refractive index mismatch [39] so a different PSF was calculated by the software for the deconvolution at different depths in the image volume. The increase in resolution which may be gained from the deconvolution process is visible in Figure 3.2b.

3.2.6. Analysis of Particle Coordinates

Density Profiles

Density profiles were calculated by counting the particles in bins along z of height less than half a particle diameter. The particle dimensions measured by TEM may be used to convert number densities to volume fractions but in this report, densities are plotted in particles per unit volume as the polydispersity of the system could make such volume fractions misleading. Conversions are made for comparison to simulations in the text. Coarse graining was carried out by convolving the raw profile with a rectangular function of width 2-2.5 µm. Where possible, density profiles were averaged over several confocal image volumes in adjacent regions.

Nematic Order Parameters

Two nematic order parameters were utilised in this investigation. The first is the one to which the term generally refers: the largest eigenvalue of the tensor order parameter, $\mathbf{Q}$ [40]:

$$\mathbf{Q}(z) = \frac{1}{N_b} \sum_{i=1}^{N_b} \left(\frac{3\hat{\boldsymbol{u}}_i \otimes \hat{\boldsymbol{u}}_i - \mathbf{I}}{2} \right) \tag{3.1}$$

N_b refers to the number of particles in the bin centred at height z and $\hat{\boldsymbol{u}}_i$ is the unit orientation vector of particle i. $\otimes$ denotes the dyadic product and $\mathbf{I}$ is the 3×3 identity matrix. The largest eigenvalue, S_B, is associated with the eigenvector pointing along the nematic director, or average orientation of the particles in the region (bin). S_B ranges from 0 in a large sample of the isotropic phase to 1 for a fully aligned set of particles.

The second parameter is a local one used by Cuetos and Dijkstra to study nematic clustering [41]. In this case a separate value is calculated for each particle based on the orientations of those close to it:

$$S_L(i) = \frac{1}{n_i} \sum_{j=1}^{n_i} \left(\frac{3}{2}|\hat{\mathbf{u}}_j \cdot \hat{\mathbf{u}}_i|^2 - \frac{1}{2} \right) \tag{3.2}$$

Here, n_i is the number of neighbours of the ith particle and j indexes through these neighbouring particles. Which nearby particles to include were chosen by searching for particles (centres of mass) within a cylinder concentric with particle i with length and diameter approximately three times that of the particle. These were chosen by inspecting a few sample particles in a smectic phase and ensuring that the cylinder length reached to the layers in front of and behind the particle and that the diameter was such that the second nearest neighbours in the hexagonal arrangement were included.

S_L runs from 1 in a fully aligned environment to 0 for an isotropic one and further to -0.5 for a particle whose neighbours are all perpendicular to it. These values may then be plotted as a scatter plot (e.g. Figure 4.13) or average values ($\langle S_L \rangle$) calculated in bins along z (e.g. Figure 4.15a).

3.3. Estimation of the Debye Length

In order to obtain an estimate of the extent of the double layer, Equation 2.1 may be used. This requires knowledge of the ionic strength of the solvent mixture. If this is not controlled by adding salt to the solvent mixture, a measured conductivity and Walden's rule may be used to obtain an estimate of the ionic strength. This is an empirical rule which states that the product of the limiting equivalent molar conductance and viscosity of a solvent is a constant for the same electrolyte in different solutions. While the identity of the trace ions in the solvent mixture is not known, a rough estimate of the ionic strength may be made. Literature values for the limiting ionic conductivity of HCl in ethanol ($\Lambda^0_{\text{EtOH}} = 84.3\,\text{Scm}^2\text{mol}^{-1}$, $\eta_{\text{EtOH}} = 1.08\,\text{mPa s}$ [42, 43]) were used along with a viscosity of index matched glycerol water mixture of $\eta_{\text{GW}} = 79.3\,\text{mPa s}$, based on a quadratic fit to an Arrhenius plot of the data in Reference 44.

$$\Lambda^0_{\text{EtOH}}\eta_{\text{EtOH}} = \Lambda^0_{\text{GW}}\eta_{\text{GW}} \tag{3.3}$$

4. Results and Discussion

4.1. Particle Synthesis

The synthesis of suitable particles was in this case a means to the end of investigating their phase behaviour. For this reason, the experiments which are presented in this section are not systematic scans of free parameters but rather educated stabs at the conditions required to make high aspect ratio fluorescent rods with sufficient non-fluorescent shell thickness for clear confocal imaging.

4.1.1. Reagent Concentration

It is known that decreasing the concentrations of either water or ammonia results in longer rods, without major effects on the diameter [21]. However, long rods can become bent or even curly which should be avoided. The effects of altering the reagent concentrations may be seen from Table 4.1 (CT1-4) and Figures 4.1(a) and (b), all of which were synthesised at room temperature with other reagent concentrations constant (Section 3.1.1).

Comparison of the CT1 and CT2 measurements indicates how sensitive the reaction is to the ammonia concentration, given that a 2 mL increase (in 800 mL pentanol) reduced the aspect ratio from 14.36 to 5.57. It should be noted, however, that the resulting particles are additionally affected by uncontrolled and poorly understood factors which mean that a repeated synthesis does not yield exactly the same particle dimensions. Since CT2 was synthesised two weeks later than CT1, using the same ammonia bottle, it is possible that the decrease in length is also in part due to additional ions that dissolved in the ammonia solution during this time. The intermediate water and ammonia concentrations used in the synthesis of CT3,4 were found to yield straight rods with workable aspect ratios.

4.1.2. Reaction Temperature

The fact that rods grown at elevated temperatures results in longer, thinner particles was noted by Kuijk [21] and further demonstrated by Datskos and Sharma [45]. They attribute the change to a decreased diameter at increased temperature and an increase in length such that the volume of TEOS contributing to each particle is approximately the same. CT5 was synthesised using the same reagent concentrations as CT3, but was incubated at 30°C for the duration of the reaction. This slightly elevated temperature was chosen to slightly increase the length of the

Name	Water (g)	Ammonia (cm^3)	TEOS (cm^3)	L (σ_L) (µm)	D (σ_D) (nm)	L/D
CT1	20	16	8	3.02 (18%)	210 (19%)	14.36
CT2	20	18	8	1.70 (16%)	305 (26%)	5.57
CT3	19	17	8.5	2.12 (21%)	226 (17%)	9.38
CT4	19.5	16.5	8.5	2.20 (18%)	226 (26%)	9.73
CT5	19	17	8.5	3.22 (20%)	209 (30%)	15.41

Table 4.1.: Altered reagent concentrations and resulting core rod dimensions. All reactions were carried out at room temperature with the exception of CT5 which was incubated at 30°C. σ_L and σ_D refer to the polydispersities in length and diameter respectively (standard deviation divided by the mean of the size distribution).

(a) CT1   (b) CT3   (c) CT5
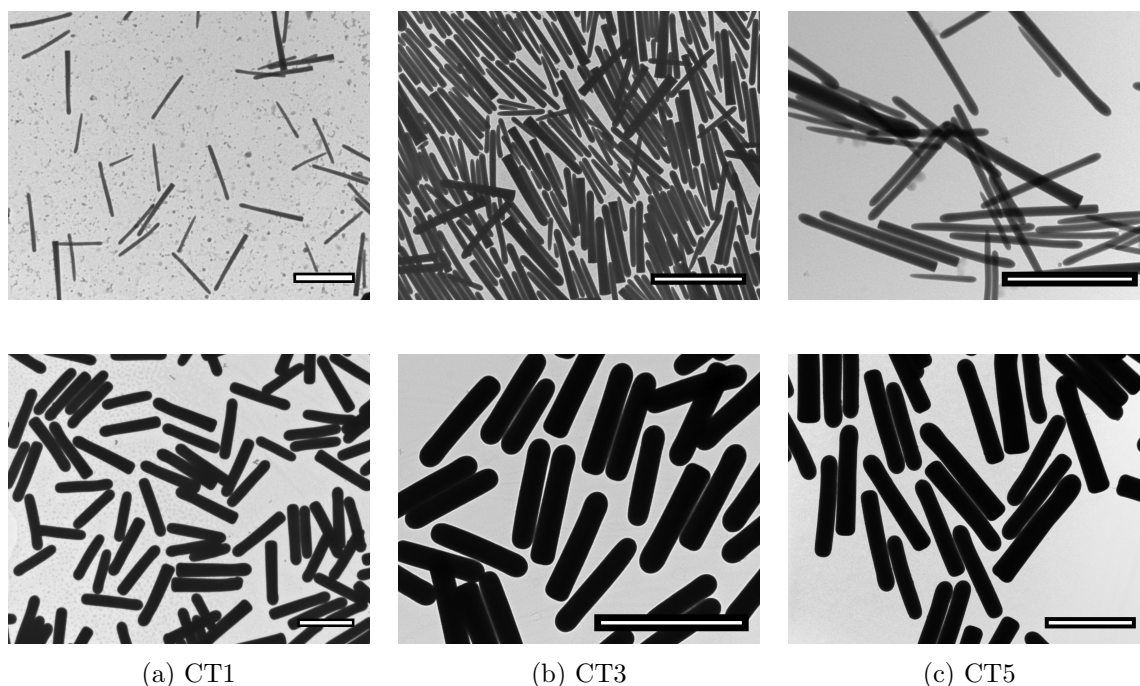
Figure 4.1.: TEM images of core (top) and fully coated (bottom) particles. All scale bars (white) are 3 µm.

particles without them becoming too long and becoming curved (see Figures S2 and S3 in Reference 45).

This resulted in an increase in aspect ratio from 9.38 to 15.41. The expected improvement in length uniformity and diameter polydispersity was not found. This is thought to be due to the fact that this reaction (as all the others) was carried out in a 1L reaction bottle, providing adequate space for disruptive convection currents to be set up. Not only would these result in different temperatures at different points in time and space but motion of the water droplets could cause diameter fluctuations during growth.

4.1.3. Shell Coating

The growth of shells around the rods was necessary for confocal microscopy but comes at the expense of aspect ratio as may be seen from Figure 4.2. How thick a shell is sufficient is discussed further in Section 4.2.3 but the lower limit is is somewhere in the region of 200 nm (including both fluorescent and non-fluorescent shells). With this in mind, examination of Figure 4.2 shows the large increase in core aspect ratio (at 0 nm shell) which is required for a small increase in aspect ratio after addition of a 200 nm shell. Due to the projected final L/D of CT2 of approximately 3, it was not coated or used for confocal studies. CT5 was used, with a similar curve to CT1 and final dimensions shown in Table 4.2.

In terms of the coating procedure itself, the first (fluorescent) shell coating was found to be the most problematic, resulting in irreversibly aggregated rods approximately half of the time. This is thought to be due to particle overconcentration, resulting in rods colliding too often in the presence of the silane coupling agent, APS, causing them to fuse. An attempt was made to counteract this by diluting the rods in more ethanol during coating and this did result in very little aggregation but a substantial quantity of secondary nuclei were also observed. This is also intuitive in that if the rod concentration is too low, much of the TEOS will not necessarily be near any rods and will nucleate spontaneously and form small (non fluorescent) silica spheres instead of being incorporated into the rods.

The formation of aggregates is known to also be heavily dependent on the ion concentration
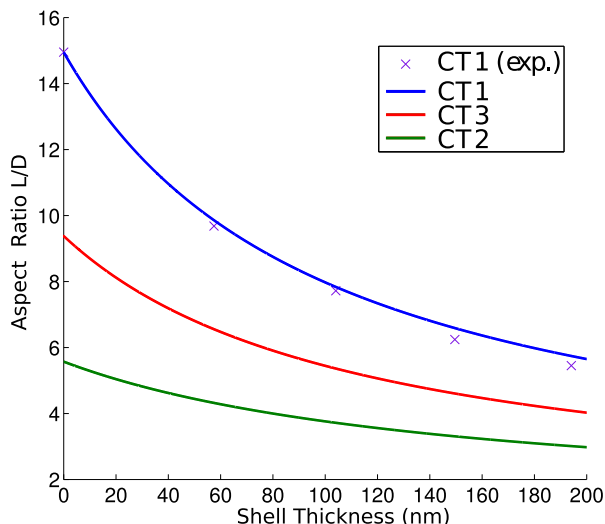
Figure 4.2.: Theoretical decrease in aspect ratio as a function of the shell thickness for CT1,2,3. Experimental data are shown for CT1 for comparison. Only CT1 data is shown as rods were removed from the others to decrease polydispersity between shell coating steps so measured shell growth data are not meaningful in this sense. The CT1 curve begins at a higher aspect ratio than shown in Table 4.1 as some small particles were removed before centifugation, driving the mean L/D up to around 15.

Name	L (σ_L) (µm)	D (σ_L) (nm)	L/D	F-Shell (nm)	NF-Shell (nm)	l_g in GW (µm)
CT1	3.38 (11.8%)	631 (7.3%)	5.36	58	137	0.53
CT3	2.60 (11.3%)	550 (9.0%)	4.73	55	126	0.92
CT5	3.77 (9.3%)	647 (8.8%)	5.83	>60	>100	0.45

Table 4.2.: Final dimensions of particles which were coated for confocal microscopy. F and NF refer to fluorescent and non-fluorescent silica shell thicknesses and GW to glycerol/water solvent (Table 3.1). The shell distribution in CT5 is not well known as it had two fluorescent shells grown around it and additional TEOS was added during the second in an attempt to prevent aggregation.

which is primarily affected by the ammonia (both by the intended catalytic and stabilising ammonium ions and by other, less welcome solvated ions which result from exposure of the stock solution to air). So it seems that a balance must be found in the particle concentration between the too concentrated and too dilute limits during fluorescent shell coating with an eye on the amount of ammonia added and the vintage of the bottle it is added from. TEOS also forms ionic species upon hydrolysis and this is likely to cause a large initial increase in the ionic strength of the mixture before a substantial quantity of silica has precipitated. In this investigation it was sufficient to simply remove the secondary nuclei by centrifugation but this unfortunately means that the optimal particle concentration was not found. Sonication during the coating procedure may be a way to reduce aggregation during this step.

The non fluorescent shell coatings were much less affected by aggregation due to the absence of APS but secondary nuclei were still sometimes formed and had to be removed before the next shell coating or index matching.

The polydispersity of the final particles should be reduced by removing large and small particles after the first (fluorescent) shell coating. This is because the polydispersity of particles is known to decrease as shell coatings are added, meaning that with more shells the particles separate less in a centrifugal field. Expending effort reducing the polydispersity before the fluorescent shell coating is inefficient in the case that the particles aggregate and are lost during

this step.

4.2. Optimisation of Confocal Imaging in Sediments of Colloidal Silica

The desire to explore the richer phase behaviour in the higher aspect ratio region of the phase diagram meant that the non-fluorescent shell on the particles should be kept to a minimum thickness. The minimum thickness of the non fluorescent layer is dictated by the resolution of the confocal images so this resolution must be as high as possible. Everything along the optical path can affect image quality, meaning that a complimentary combination of lens/immersion fluid/viewing window/dispersion must be found.

4.2.1. The Lens and Cell Viewing Window

Figure 4.3 shows the results of the lens testing on the $L/D = 4.7$ particles.

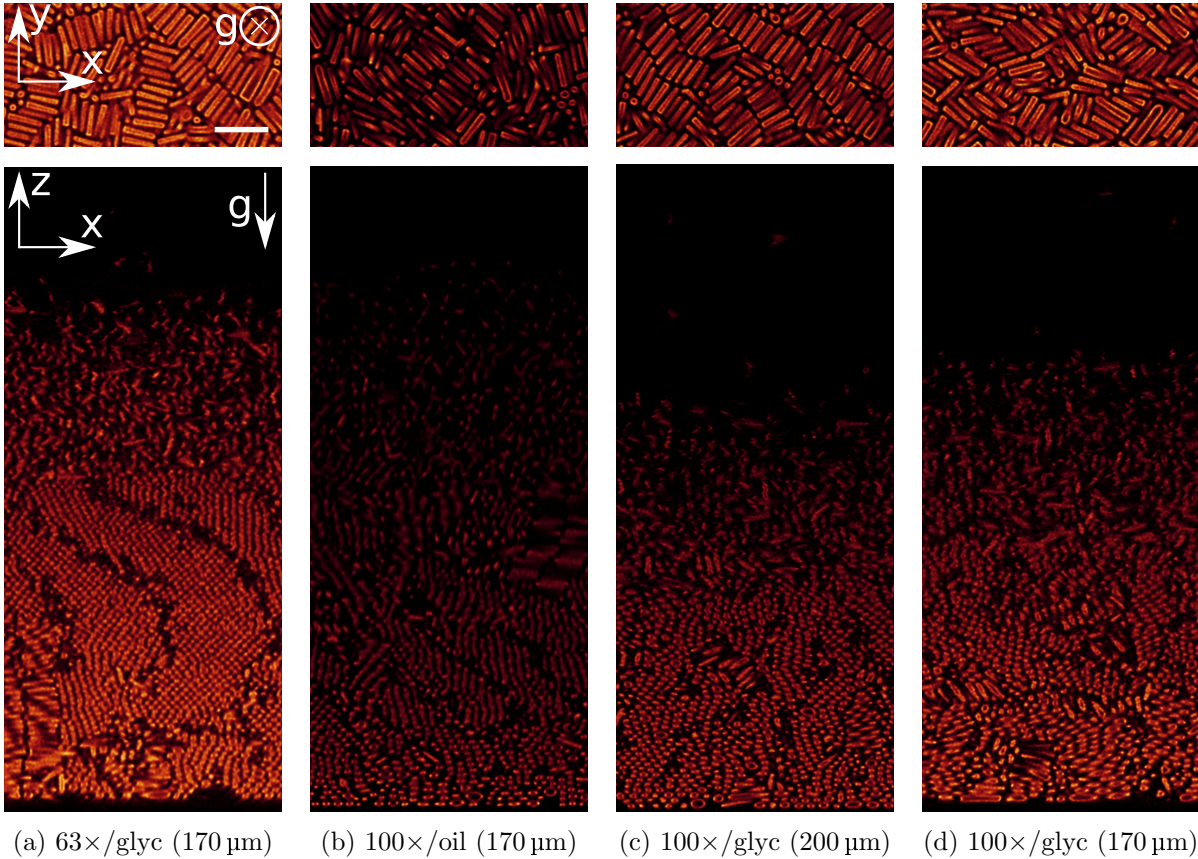(a) 63×/glyc (170 µm)   (b) 100×/oil (170 µm)   (c) 100×/glyc (200 µm)   (d) 100×/glyc (170 µm)

Figure 4.3.: Deconvolved images of sedimentation profiles obtained with different lenses. The lengths in parentheses refer to the cover-glass thickness. The x-y scale is the same in all images and is conveyed by the 5 µm scale bar in (a). All images in x-z are approximately 100 µm high.

Comparison of Figure 4.3b to the others, (particularly Figure 4.3a as these show the same cell) makes clear the improvement in intensity high in the sample of the glycerol immersion lenses. A slight decrease in the rate of intensity drop-off is expected due to the lower numerical aperture of the glycerol lens but the drastic improvement is due to the matching of refractive indices of the immersion and dispersion ($n_D = 1.45$) media [39]. The higher resolution (subjectively) observed in the 100×/oil lens over the 63×/glycerol one is due to the higher magnification and

numerical aperture and also to the fact that this lens is newer and has been subject to less wear than the 63×/glycerol one.

The 100×/glycerol lens is built for use with quartz coverslips (n=1.46 [46]) which means that the immersion/coverslip/dispersion all have almost identical refractive indices, representing a theoretically ideal set up. Figures 4.3c and 4.3d did indeed show improved resolution and intensity distribution along z compared to the oil lens. Improved resolution at very low z is not predicted by the lower NA of the 100×/glycerol lens so it is thought that this gain in resolution at the bottom is due to the use of the correction collar which can have the effect of correcting for a slight index mismatch of the solvent mixture. Higher in the sample, the improved resolution of the 100×/glycerol lens is principally due to the refractive index match. In literature, it has been shown that the mismatch between an oil immersion lens and an $n_D = 1.47$ medium (close to the case here with $n_D = 1.45$) causes resolution and intensity to drop by a factor of 1.2 and 30% respectively per 10 µm of z increase [39]. In the absence of this mismatch effect, the glycerol lens has a much lower rate of resolution decrease with height.

The effect of the cover-glass thickness on the performance of the 100×/glycerol lens was tested by building two cells with with quartz windows of 200 µm (Figure 4.3c, recommended by the manufacturer) and 170 µm (4.3d). The intensity decrease appears to occur at the same rate with both cover-glasses but the resolution difference, if there is one, is difficult to determine. The many different rod orientations observed in the 170 µm sample makes this image appear to have the poorer resolution but this should theoretically not be the case as in a fully index matched optical path the coverslip should be 'invisible' to light passing through it, not affecting its direction at all.

It is concluded that the two 100× lenses are both suitable for capturing high quality images for particle coordinate extraction, depending on the sediment height. For low sediments, the oil immersion lens is most convenient due to the readily available borosilicate cover-glasses that it is optimised for. For sediments higher than 50 µm where particle fitting becomes difficult with oil immersion images, the glycerol lens may be used. Use of either 200 or 170 µm cover-glasses is possible with the latter being the most expensive but providing the largest working distance (approximately 170 µm).

4.2.2. The Solvent Mixture

The basic requirements for a good dispersion medium for this investigation are a matched refractive index to the colloidal silica and sufficient polarity to disperse the negatively charged particles. Like microscope objectives, different solvent compositions also have different advantages and disadvantages which in this case are related to their viscosities and interactions with the components of the cell.

Mixtures of dimethyl sulfoxide (DMSO)/water and glycerol/water have been used previously to index match these particles [21]. These were both also used in this investigation. The low viscosity of the DMSO based mixture ($\eta^{25}_{10\%H_2O} = 2.70\,\mathrm{mPa\,s}$ [47]) is such that the particles sediment quickly and undergo rapid Brownian Motion. This is convenient because it means that an equilibrium sediment may be obtained in a matter of days. Diffusion is also rapid which means that very fast imaging is required to capture large fields of view in the isotropic phase without the images being affected by motion blur. Another disadvantage is that DMSO is known to react unfavourably to the sample cell. It has been noted previously that it reacts with UV curing glue, forming dispersions of the glue in the sample which is undesirable [33]. This may be circumvented by sealing the sample cell with candle wax but this is not a permanent solution either. It was found that in cells sealed at the bottom with candle wax followed by UV glue leaked within a few weeks of the addition of suspension.

Cells containing glycerol/water mixtures were found to be stable indefinitely, remaining sealed for several months. However, due to the high viscosity of the mixture ($\eta = 109.9\,\mathrm{mPa\,s}$ at 20 °C
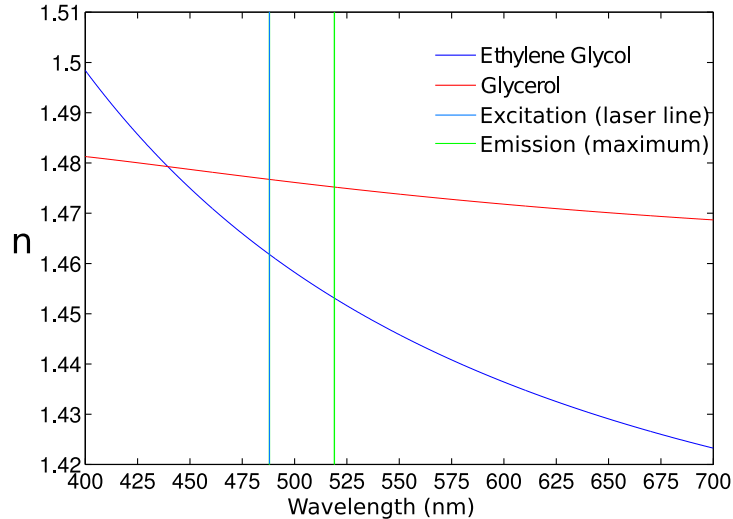
4. Results and Discussion

Figure 4.4.: Dispersion relations for Ethylene Glycol (blue, 20°C) and Glycerol (red, 25°C). The wavelengths of the laser excitation line and FITC peak emission are marked as blue and green vertical lines. Based on literature Cauchy coefficients in [48] and [49].

[44]) sedimentation and equilibration take several weeks. An advantage of this is that the dynamics are very slow and clear images may be captured even in the isotropic phase. For these reasons of long term stability and ease of imaging, this solvent mixture was chosen as the principal one for sedimentation experiments.

Two other solvent compositions were investigated in order to try and find one with a viscosity, and hence dynamic time scales, between those of DMSO and glycerol based solvents. The first of these was ethylene glycol (EG) ($n_D^{20} = 1.439$ [48]) with DMSO added to increase the refractive index. However, when CT1 particles were transferred into EG, it was found that the refractive index could not be matched by eye with additional DMSO. The reason for this is likely to be that EG has relatively high optical dispersion in the visible range. A comparison of the refractive index dependence on wavelength is shown in Figure 4.4.

It may be seen that the variation in refractive index across the visible range is so large that it is unsurprising that an index match could not be found by adding DMSO. The refractive index at the relevant wavelengths is in fact very close to matching the silica so it is possible that lowering the index with water would have been more fruitful. However, the variation between the refractive indices around the excitation and emission wavelengths (vertical lines) is also significant which is undesirable in a confocal solvent medium as it would introduce a difference in the optical paths of excitation and emission light. Therefore the use of this solvent was not investigated further.

Another possibility was to decrease the viscosity of the glycerol/water mixture by adding DMSO and adjusting the water concentration accordingly. An index match was achieved with this mixture and its viscosity was measured to be around $30\,\mathrm{mPa\,s}$, which would result in the desired intermediate dynamic time scales. However, imaging of this mixture was found to deteriorate over time in wax sealed cells. The reason for this is unknown but the leakage of wax sealed DMSO/water cells suggests some reaction between DMSO and candle wax which could result in a change in refractive index of the medium. None of these cells were observed to leak though and the $L/D = 4.7$ results in Sections 4.4.2 and 4.6 were obtained using this solvent.

4.2.3. Feature Fitting in the Sediment

The accurate fitting of particles in concentrated phases such as those found at the bottom of the sediment is much more difficult than in dilute suspension due to the overlapping fluorescent

signals. This overlap may be decreased by growing non-fluorescent silica shells around the particles and by deconvolving the confocal images. In order to investigate systems of high aspect ratio, thin non fluorescent shells were grown and deconvolution used in all cases. Even after deconvolution it was often found that an unsatisfactory fraction of the particles could be fitted. For this reason it is thought that the non fluorescent layer of around 130 nm on the particles in this research is the lower limit of thickness providing sufficient separation for single particle tracking. It was found that the same particles in different solvents/cells could only some of the time be satisfactorily fitted but that when a cell could be fitted once, it could be again. This is demonstrated by the example in Figure 4.5 corresponding to the discussion in Section 4.5 which was fitted accurately after 12, 47 and 90 days, despite some photobleaching during this time. Therefore it seems that the factors which push these thin shelled particles to and fro over the 'fittable border' is something which remains constant in a cell, ruling out temperature fluctuations which are known to affect solvent refractive indices. For a constant non-fluorescent shell thickness (i.e. the same batch of particles), the principal suspects are the cover-glass thickness (which can vary within a few µm of the stated and optimal value), the refractive index match of the solvent due to its composition and differences in ionic strength between solvent mixtures. The latter factor would cause differences in the double layer thickness of the particles and hence affect their separations. This should be taken into account when considering the necessary thickness of non fluorescent shells, as comparisons are most meaningful when the solvents and ionic strengths are the same.

The Dense Isotropic

In a system such as that shown in Figure 4.5, with a hexagonal phase lower down and an isotropic phase above it, the dense isotropic/coexistence region is the most difficult area for particle fitting. This is because low in the sediment, the hexagonal layers are mainly oriented such that the particles lie in the xy plane with ABA stacking along z. This means that the particles are well separated by the spaces in an intervening layer of particles along the z axis, along which the limiting resolution of confocal microscopy is.

Particles in the dilute region do not have overlapping fluorescent signals so may be easily found. However, in the dense isotropic, many particles have a component of their orientation along z and the separation of particles in this direction is not well regulated. This results in blurring of the signals together which makes distinguishing them difficult.

As this region is crucial to the study of the phase transition, great care must be taken to ensure that the particles located here are fitted successfully, or at least that the fraction of missed particles is the same as that in the rest of the sediment.

4.3. The Isotropic Phase

In order to justify the use of the particle fitting method discussed in Section 3.2.4 on sediments, the same method was applied to an isotropic suspension of CT1 in index matched glycerol/water ($\phi \approx 3\%$). In such a system, there is no positional or orientational ordering and particles are distributed uniformly through space with random orientations. For this reason, it is an ideal case with which to test for biases or artefacts in a particle fitting method.

Sedimentation was avoided by rotating the sample for two weeks (in a capillary-like arrangement constructed from cover glasses, see for example Figure 6A in Reference 30) and imaging soon after removal from rotating stage [50]. In addition to removing particles at the sides of the box, particles at the bottom were also discarded such that the few particles which had sedimented to the glass slide were not included. Figure 4.6a shows a 3D computer rendering of the 363 fitted particles. After visual verification of the fit result overlayed onto confocal images (as in Figure 3.2d), inspection of the 3D rendering is a good starting point to look for obvious
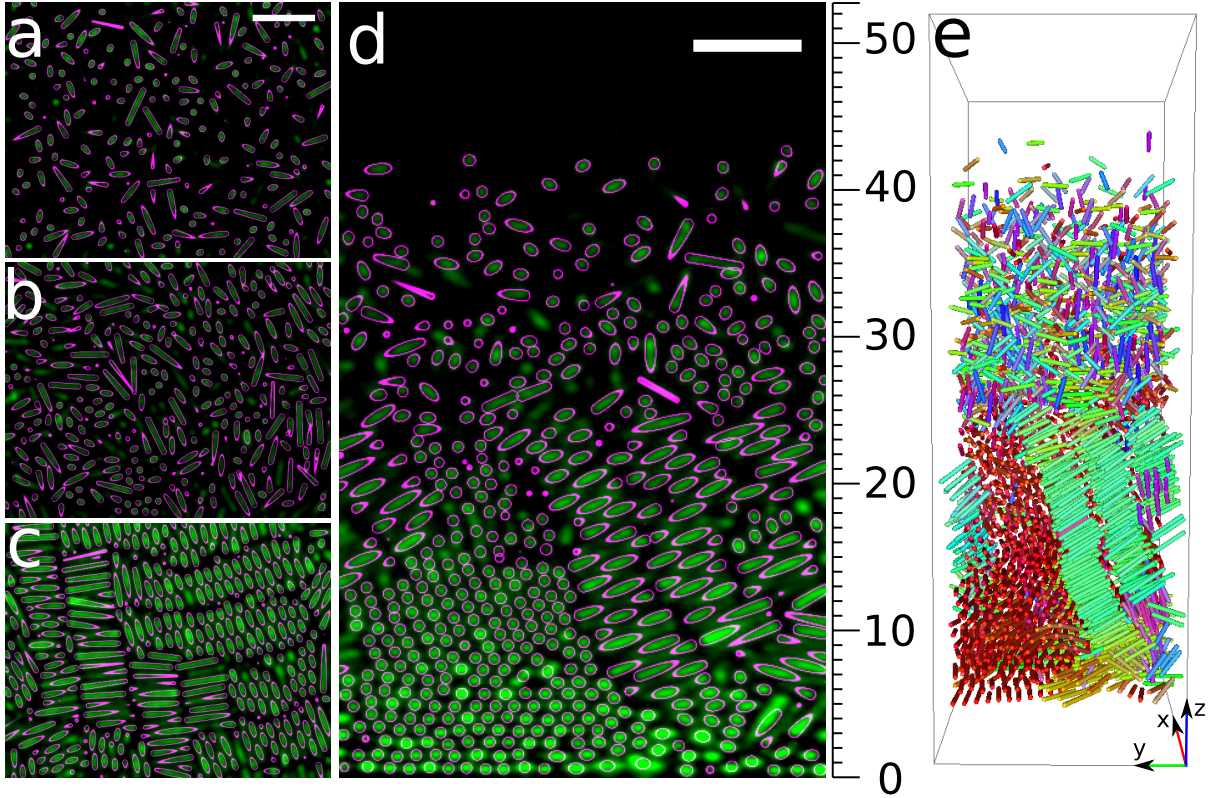
Figure 4.5.: Feature fitting of one stack imaged after 90 days in which 5031 particles were found. x-y slices of the overlay are shown at (a) 38 µm (b) 26 µm (c) 12 µm. (d) shows a slice in y-z with the corresponding computer rendering from the fitted particles in (e). Scale bars are 5 µm and refer to the x-y scale. The z scale is indicated by the µm ruler.

anisotropies or artefacts. These might include one colour (orientation) being over represented or a sedimentation profile arising. This image does indeed conform to the expected appearance of an isotropic system.

In order to quantify the degree of orientational order, the local order parameter was calculated for each particle and is shown in Figure 4.6b. It may be seen form the many blue points that all of the particles are in disordered environments (mean $S_L = 0.012$). The reason for the broad distribution between -0.5 and approximately 0.2 is due simply to the local nature of the calculation which does not always include enough particles to for the order to decay entirely. The few particles which are found in apparently higher order environments are alone and in random locations, so are not part of any kind of ordered domain but simply due to random fluctuations. This is not unexpected in a snapshot of a Brownian system such as this one.

4.3.1. Effects of Data Processing on Results

As there are a large number of analysis steps, often with several tunable parameters, between confocal imaging and the extracted particle coordinates, it is important to verify that these are not artificially altering the results. The three most likely to introduce false anisotropy or bias into the system are the deconvolution, blurring of the images and the way in which the voxel aspect ratio is taken into account. To test the effects of each of these, four slightly different analyses were applied to the same image volume as shown in Figure 4.6a. The standard parameters were those typically used on sediment images and were therefore a compromise between those optimised for concentrated and dilute regions. An anisotropic Gaussian blur with
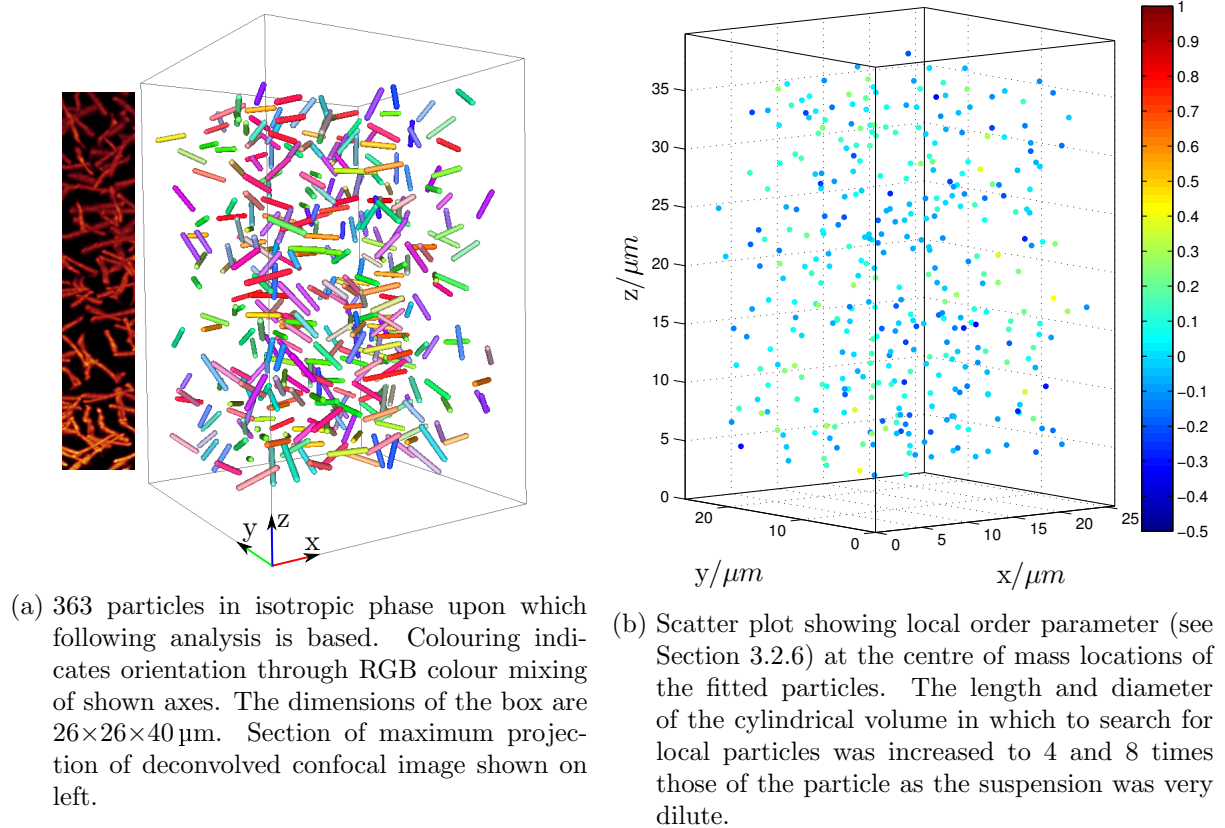
(a) 363 particles in isotropic phase upon which following analysis is based. Colouring indicates orientation through RGB colour mixing of shown axes. The dimensions of the box are $26 \times 26 \times 40\,\mu$m. Section of maximum projection of deconvolved confocal image shown on left.

(b) Scatter plot showing local order parameter (see Section 3.2.6) at the centre of mass locations of the fitted particles. The length and diameter of the cylindrical volume in which to search for local particles was increased to 4 and 8 times those of the particle as the suspension was very dilute.

Figure 4.6.: Isotropic suspension of CT1 obtained by continuous rotation for two weeks to counteract the effect of gravity and hence prevent sedimentation.

diameter 3.4 pixels in xy ($\sim 0.25D$) and 1.9 in z ($\sim 0.13D$) was applied to the deconvolved image volume and the pixel aspect ratio was taken into account (the imaged voxel had dimensions $51 \times 51 \times 84\,$nm) by scaling the coordinates along z after fitting.

Small differences were separately made to the fitting parameters to investigate their effect: an isotropic blur of diameter 2.3 pixels, scaling the images up and interpolating before fitting and applying the original fitting parameters to raw data (without deconvolution). The locations were found to be visually very similar in the overlay. The density profile resulting from each is shown in Figure 4.7. It may be seen that the deviations between the profiles is largest at high z. This is due to the decreased signal high in the imaging volume as can be seen from Figure 4.6a. Therefore it is concluded that the fits applied here are similar enough to be equivalent but a higher uncertainty is present at high z, when imaging the same phase.

Another important thing to know is whether or not the digital nature of the imaging process results in biasing of coordinates towards or away from integer pixel values. This was tested by transforming the coordinates from µm into pixels and plotting a histogram of the fractional parts (Figure 4.8a) and checking for systematic tends. The low number of particles (363) in this volume means that these plots are necessarily noisy. However, there does not appear to be any significant biasing towards 0 or 1 in any of the different fits. The differences between the bars for different parameters in this case are not relevant as very small differences in positions can cause such a plot to look completely different.

Figure 4.8b shows the distribution of orientations and here the bars for different fits should be the same as small deviations in orientation would still fall into the same bin. This does appear to be the case, except for the highest values of $|u_z|$ (corresponding to rods pointing straight upwards). All seem to be slightly biased against this orientation except for the fit to non deconvolved data.
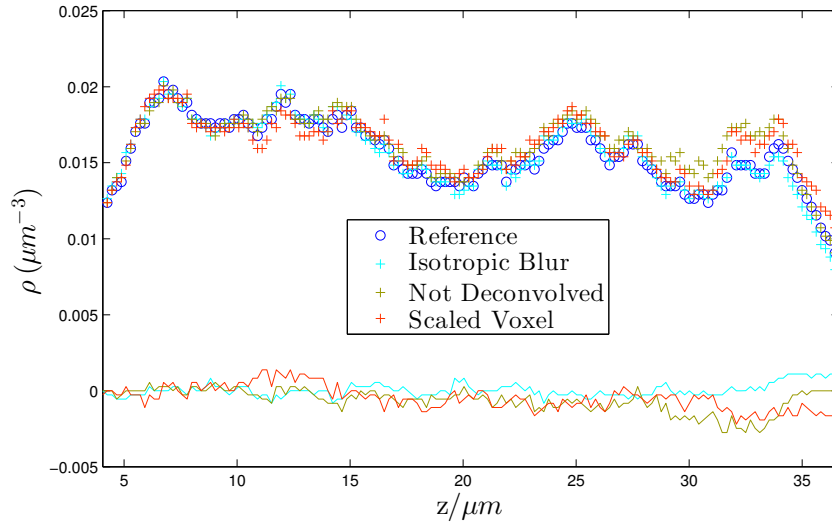
4. Results and Discussion

Figure 4.7.: Coarse grained density profiles of an isotropic suspension obtained using different analysis parameters. Difference plots with respect to the reference are shown as lines. The slightly higher density at low z shows that some sedimentation has already occurred. The tails at the edges are due to coarse graining across the empty edges where particles have been discarded.
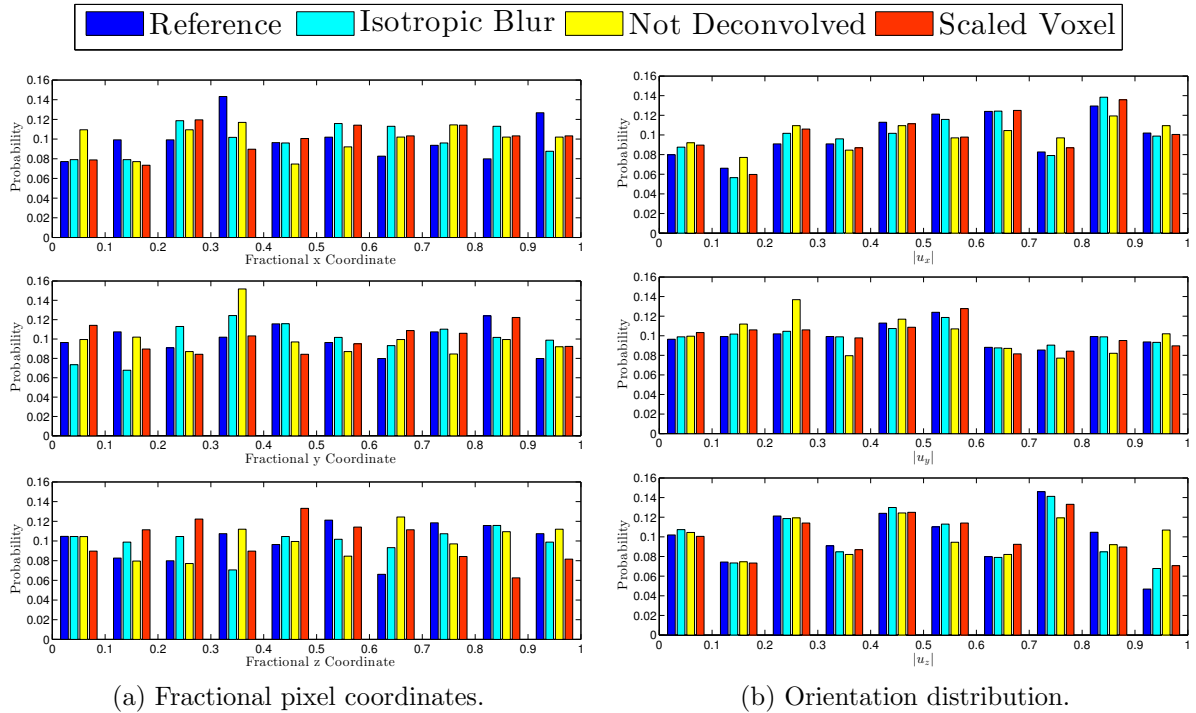

(a) Fractional pixel coordinates.

(b) Orientation distribution.

Figure 4.8.: Fractional pixel coordinate plots.

4.4. Phase Observations in the Sediment

4.4.1. The Systems

The sedimentation profiles of two systems are presented in this section, one with particle aspect ratio 5.4 (CT1) and the other with aspect ratio 4.7 (CT3). The preparation of the cells of which the results are shown here are different (sedimentation from the top and from the bulk respectively) but the results for CT3 are typical of those found for CT1 under similar conditions, but these are not shown to avoid repetition.

L/D=5.4: Sedimentation from the Top

The sedimentation profile was obtained by adding $5\,\mu L$ of CT1 ($\phi \approx 3\%$) suspension in GW solvent to the top surface of $345\,\mu L$ of the same solvent in a cell. The solvent was index matched by eye and the salt concentration was not controlled in this case. Confocal image stacks were obtained after 6, 12, 47 and 90 days. The appearance of the sediment did not change after 12 days so is thought to have reached equilibrium by this time. This is somewhat sooner than would be expected based on the sedimentation velocity calculated from Equation 2.8 of $341\,\mu m/day$ ($20\,°C$) with a cell height of approximately $1.2\,cm$ and the large decrease in sedimentation velocity with increasing volume fraction [51]. This rapid sedimentation is attributed to Rayleigh Taylor like instabilities which form when a concentrated colloidal dispersion is added to a solvent devoid of colloidal particles [52]. However, the macroscopic properties of the equilibrium sediment should not be affected by the sedimentation mechanism.

The results presented in this section are those obtained by imaging after 90 days. 24 stacks with dimensions $26\times20\times53\,\mu m$ (voxel: $51\times51\times84\,nm$) were captured in adjacent regions. The image volumes were deconvolved and the particles fitted for each stack. Figure 4.9 shows a small section of the merged volume.

L/D=4.7: Sedimentation from the Bulk Isotropic

The images presented are of the sediment used to test the $100\times$/glycerol lens (details in Section 3.2.3), 67 days after the cell was filled. This was assumed to be in equilibrium as particles in glycerol/water were observed to equilibrate in shorter times than this and the solvent in this case (GDW) has a lower viscosity.

4.4.2. General Form

The general form of the sediment may be ascertained from Figures 4.9, 4.10 and 4.11. The dilute isotropic region at the top gives way to a hexagonally ordered phase as the density increases. This is indicative of three possibilities: a crystalline, columnar or smectic-B phase. Determination can be aided by 3D reconstructions, either from particle fitting or rendering the confocal image intensities as shown in Figure 4.12 (a-c). Figures 4.12b,c show different views of the turquoise particles in Figure 4.12a. In Figures 4.12b,c three layers of particles whose projections overlap with each other are shown, indicating AAA stacking. Figure 4.12a confirms this and gives an idea of how well defined the smectic layers are. The layering is certainly defined, which is indicative of the crystal but there are some particles which are displaced out of the layers. Therefore this region shows an arrangement intermediate between that of the crystal and columnar phases. Similar AAA stacked regions were found in a few different areas of the sediment but frequently it was not possible to confirm interlayer correlation. This was sometimes due to a changing director (Figure 4.10b) but in the case of Figure 4.10c, the well defined layers appear to be part of a smectic-B phase.

Neither the nematic or smectic-A phases were observed, in contrast to predictions by computer simulations for this aspect ratio. The top of the concentrated part contains large hexagonally
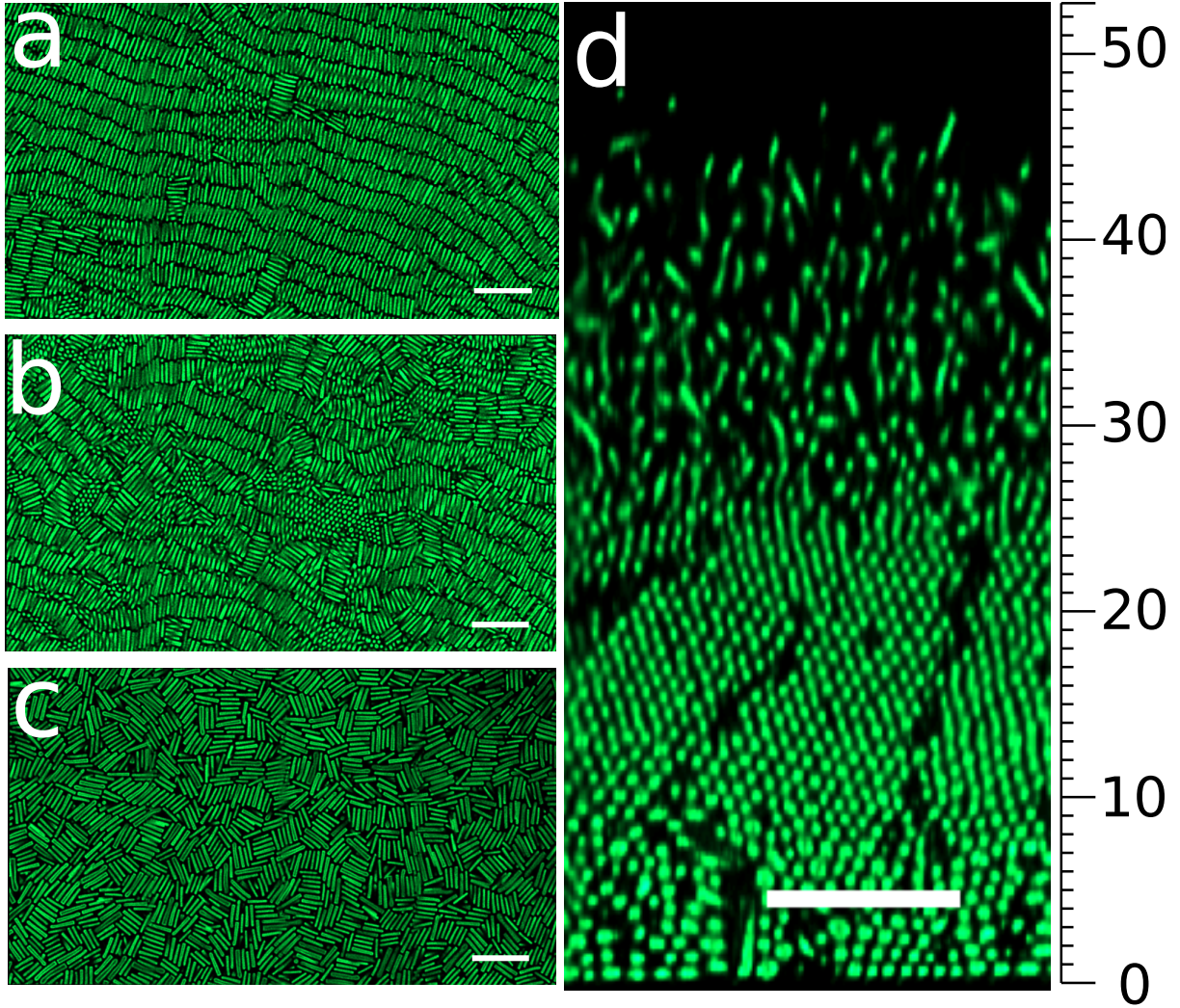
Figure 4.9.: Phases of $L/D = 5.4$ rods from confocal images. x-y views at (a) $20\,\mu$m (b)$10\,\mu$m (c) $0\,\mu$m (at the glass slide) (d) z slice showing full sediment against a scale of microns. The contrast of a,b,d was artificially increased for better visualisation here but this is not applied during the particle fitting procedure. All scale bars are $10\,\mu$m.

ordered domains close to the interface but the size of these domains is smaller lower in the sediment, while the average size of the particles is visibly larger. Close to the glass slide, the particles are found to be in very small domains with a myriad of orientations. This behaviour is observed in both systems.

The reason for the smaller domains and lower order close to the bottom is thought to be related to size segregation through the sediment. This occurs because the larger particles sediment more rapidly and hence are found in the lower regions of the sediment. This results in a local polydispersity at the bottom which is higher than the global values of $\sigma_L \approx 12\%$ and $\sigma_D \approx 7\%$ and this likely disrupts the formation of ordered layers. Moving upwards, there are fewer and fewer large particles which means that the local polydispersity decreases, allowing the particles to form larger ordered domains.

Another factor which may affect the local polydispersity is fractionation. This is distinct from size segregation in that the particles with different sizes end up in different phase regions because their relative size is such that their incorporation into one phase is more energetically favourable than into another. In literature, extremely polydisperse particles of rod-like [53]
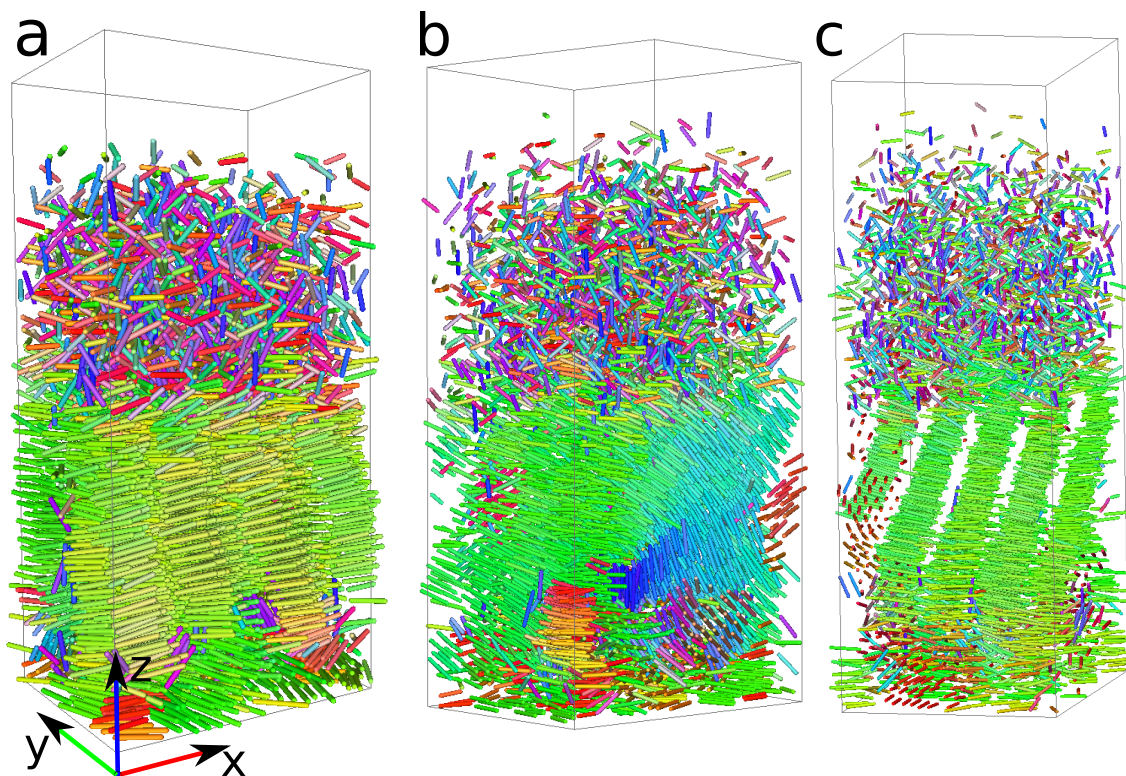
Figure 4.10.: Computer renderings of three different regions of the L/D=5.4 sample. (a) A representative region. (b) In many areas, the nematic director appears to flow through the sediment as exhibited by the blue particles. It should be noted that these particles are still in hexagonal smectic layers. (c) Smectic layering is well defined but correlation between the layers could not be confirmed so the region is identified as a smectic-B phase.

and board-like [54] goethite ($\sigma_L > 50\%$ in both cases) have been observed to form smectic-A phases. It was concluded that this was made possible by fractionation causing large decreases in the local polydispersity through rejection of all the particles with dimensions unsuited to the smectic layers to a columnar phase which can accommodate them. It is likely that this also took place in this research, resulting in the observations of both smectic and columnar phases. It should be noted however that there is more opportunity for fractionation in systems of goethite nanoparticles than in ones composed of comparatively large silica particles studied here as the goethite particles have gravitational lengths hundreds of times greater. It is therefore thought that the overall polydispersity distribution along z is governed by size segregation with fractionation acting to finely modify it at a local level, allowing formation of well defined smectic layers in many regions.

The absence of the smectic-A and nematic phases may be explained by the fact that the particles are charged and so have an electrical double layer around them. This means that the silica dimensions measured by TEM are no longer indicative of the effective dimensions of the particle [8]. Geometrically, the double layer adds to the dimensions in the same way as silica shells so this drives the aspect ratio downwards towards the ABC crystal/isotropic system which is predicted at low aspect ratio [25]. So it seems that the effective aspect ratio of this system is such that the crystal phase is predicted at high density but that it is frustrated. The frustration is likely caused by polydispersity. Length polydispersities of around 10% are predicted by simulations to disrupt the crystal towards a columnar phase [55]. Due to the removal of large particles to the bottom, it is likely that the hexagonally ordered particles have local polydispersities slightly below those quoted in Table 4.2. A local polydisperity of

slightly below 10% could explain the observed AAA stacking behaviour: the length variation frustrates the crystal slightly towards the columnar phase and this is just enough to push the layer stacking from ABC to AAA but without a full transition to the columnar phase. This is discussed further in Section 4.5.2.

The way in which the cell was prepared did not appear to affect this general behaviour,with the appearances of Figures 4.9 and 4.11 largely comparable. However, the microscopic structure of the two was somewhat different. When the particles were simply allowed to sediment out of dilute isotropic suspension, they formed hexagonal domains with directors generally either normal to or perpendicular to the glass slide. When a small amount of concentrated dispersion was added to the top of a cell filled with matched solvent, the direction of the average orientation appeared to 'flow' through different regions of the sediment (blue particles in Figure 4.10b). This behaviour is not well understood but is likely due to the way that the particles reach the bottom of the cell, with the aid of the Rayleigh Taylor like instabilities which mean that 'droplets' of colloids-in-solvent rapidly reach the bottom of the container all at once [52]. It is conceivable that remnants of this non equilibrium flow behaviour remain in the equilibrium system.

4.5. Complete Coordinates of the Full Sediment

4.5.1. Overview

Approximately 120,000 particles were found across the 24 imaged volumes, the relative positions of which may be seen in Figure 4.13a. This shows the local order parameter scatter plot from the top so mainly isotropic (blue) and very dilute (black) particles may be seen. The grid between the rectangles is due to the filtering of particles spanning the edges of the boxes. The fitting procedure was applied to each volume separately due to blurring in the overlap regions in the merged image (Section 3.2.3). Figure 4.13b makes clear the general degree of ordering at different heights in the sediment. It is found to be similar to what was concluded from examination of Figures 4.9, 4.10 and 4.11: increasing order from the bottom to highly ordered (dark red) becoming clearly isotropic at the top (light blue). Substantial variation between the heights at which the order becomes maximal may be seen. A single image volume is shown in Figure 4.13c. Here the well defined stacking of the hexagonal layers in the highly ordered central region is clear. The layering of the particles close to the bottom along z is also observable.

4.5.2. Density and Order Parameter Profiles

Apart from the convenient possibility of examining 3D reconstructions of the sediment, there is more information that may be extracted from knowledge of the full set of positional and orientational coordinates. The density profile (Figure 4.14a) is one of the most fundamental properties of the system which may now be accessed. This is calculated by sampling the number of particles in bins along the z direction with height $0.22\,\mu m$. This yields the raw number density profile which is then coarse grained with a rectangular resolution function.

The large density fluctuations in the raw profile are due to the layering of the particles close to the glass slide. Despite the fact that the layering of particles is more well defined higher in the sediment as evidenced by the hexagonal ordering, the density oscillations are only seen at low z. This is due to the observed behaviour that the layers are no longer only oriented perpendicular to gravity, meaning that z sampling does not find a single layer in a single bin.

The coarse grained profile may be used to gain an idea of the average density in a region. The density is not found to be maximal at the bottom of the sediment, where the pressure is highest. This is explained by the presence of the large particles which contribute equally to the density as an average sized particle but naturally occupy a greater volume. Higher in the sample, the density rises to a peak. This rise is thought to be due partly to the decrease in size of the particles at higher points in the sediment but also to the increase in the size of the
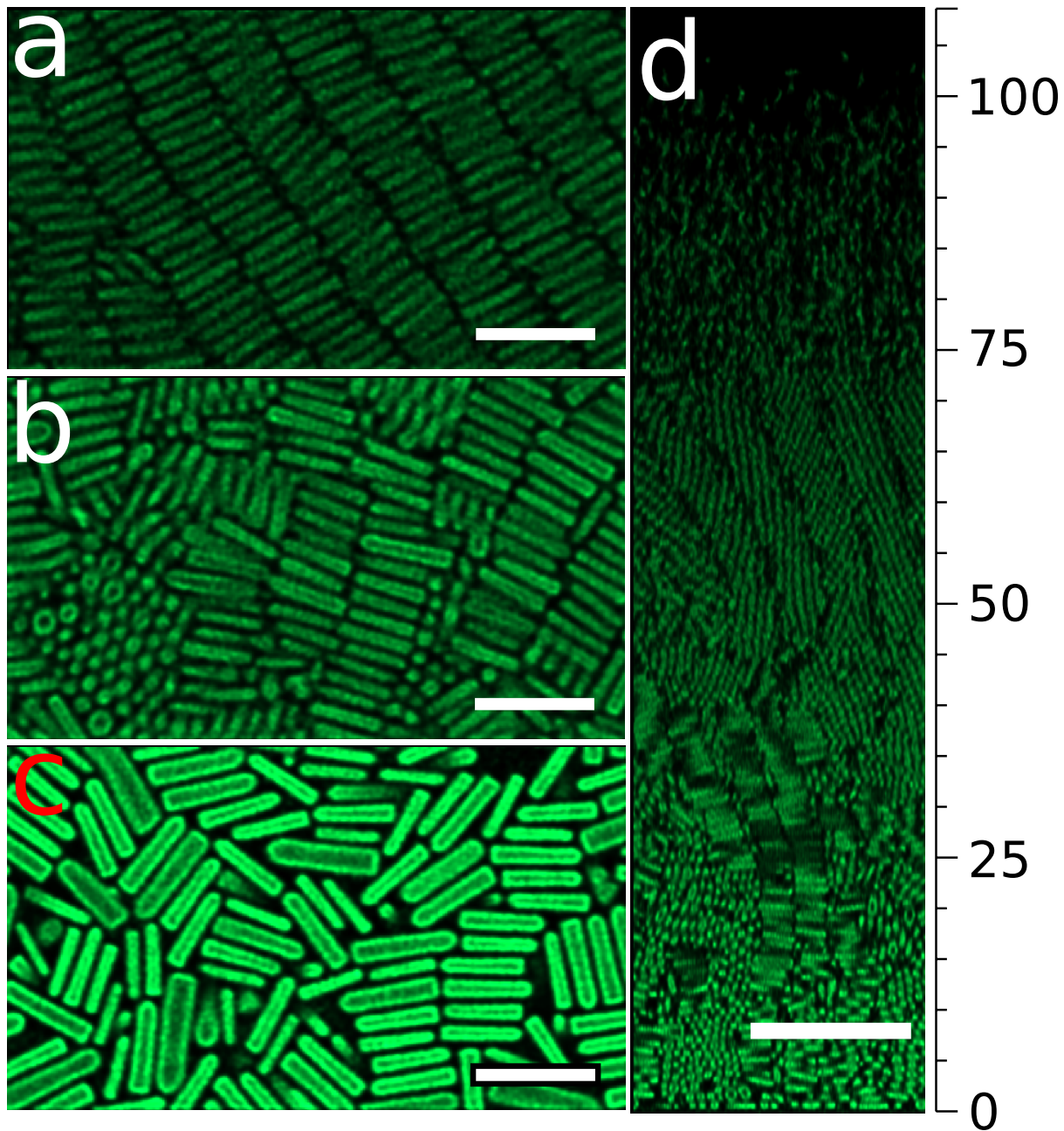
Figure 4.11.: Phases of $L/D = 4.7$ rods observed by confocal microscopy ($100\times$/glycerol lens). x-y views are shown at (a) 60 μm (b) 25 μm (c) 0 μm (at the glass slide). Scale bars are 5 μm (a-c) and 7 μm (d) and the z scale is in μm.
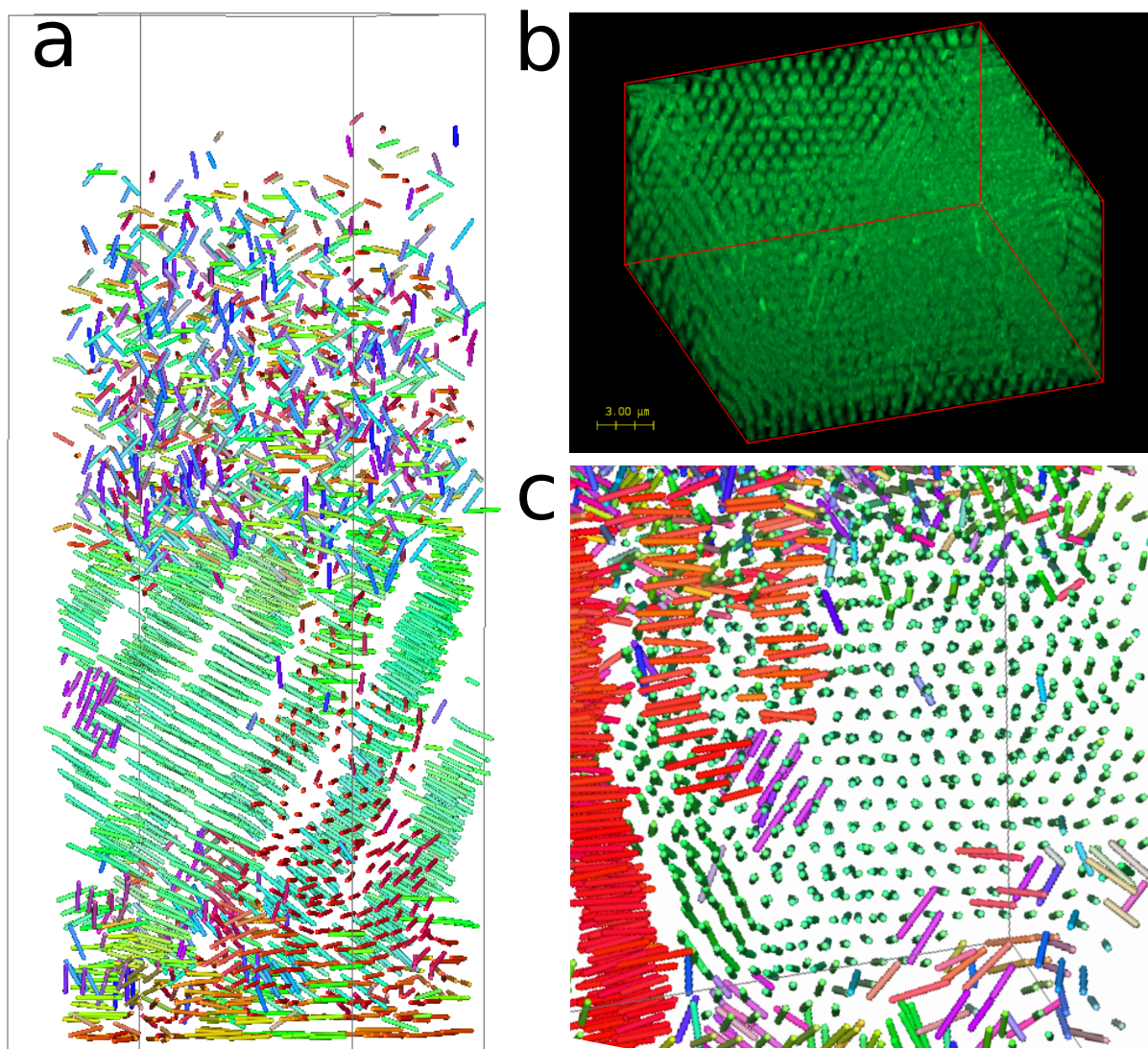
Figure 4.12.: Computer renderings of various views of the $L/D = 5.4$ fitted particles. All images show the turquoise particles in (a) which show AAA correlations between reasonably well defined layers. (b) shows a projection of the 3D confocal image volume through 3 layers and (c) shows the rendering of the same layers. The purple particles are helpful to see the relationship between the different viewing angles in (a) and (c).
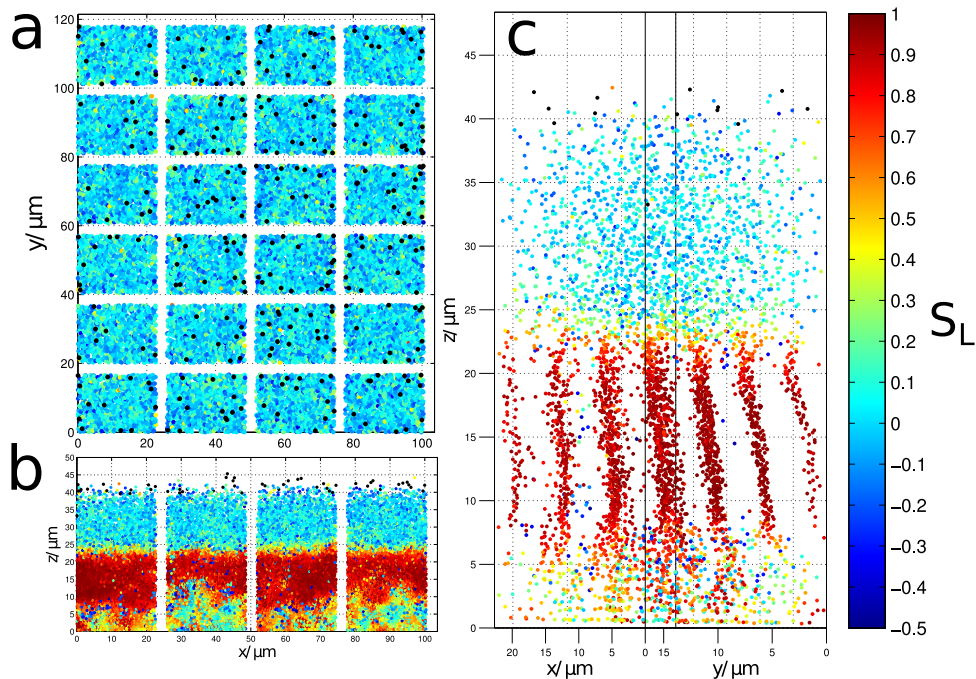
Figure 4.13.: Local order parameter scatter plots of the sedimentation profile. (a) Top view of xy plane showing arrangement of the 24 image volumes in space. (b) *x-z* view giving an impression of the order at different heights. (c) Larger view of the volume at the origin showing the well defined smectic layers. Particles with very few others nearby are shown in black.

hexagonal domains and decrease in the defect density. The density then begins to decrease at approximately 18 µm, at the onset of the isotropic phase.

The Gravitational Length from the Density Profile

The top of the isotropic region is very dilute and the situation described by Equation 2.4 is recovered. This equation may be used to obtain an in situ experimental estimate of the gravitational length of the particles in the barometric region. The gravitational length is the inverse of the decay constant of the density in this region and may be obtained by fitting an exponential function to the very dilute tail of the density profile as shown in Figure 4.14.

The log plot shown in Figure 4.14b (inset) shows three distinct regions. In the highest one, the density falls very rapidly over the space of around 1 µm. This is thought to be an artefact of the sampling of the density into finite bins. The density is necessarily quantised in whole particles and even in an averaged and coarse grained profile such as this one, the large relative change caused by a decrease in number of only one causes the macroscopic arguments leading to the barometric prediction to break down. The second region is the one of interest here: the barometric part, shown as dotted crosses, which was used for the fit. Lower than this region, the density no longer increases (moving from top to bottom) exponentially (linearly in log plot). In this region, the particles begin to interact with each other and the barometric law no longer holds. The barometric region is found here to extend to volume fractions up to 3% ($0.04\,\mu m^{-3}$). While these three regions are reasonably distinguishable, the choice of where to draw the line between them is not entirely clear and this is the reason for the relatively high uncertainty of 0.1µm in the gravitational length value.

The value of l_g obtained from this fit may be compared to the calculated value based on the rod dimensions obtained from TEM measurement. The mass of a mean sized rod was calculated
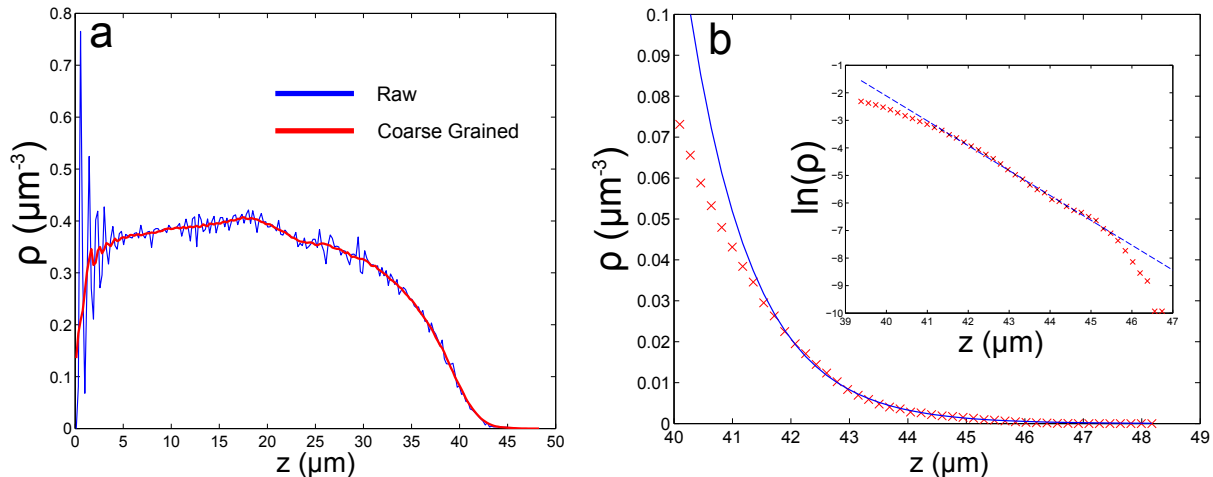
4. Results and Discussion

Figure 4.14.: (a) Blue line shows raw density profile and red line the same profile coarse grained with a resolution function of width $2.25\,\mu m$. (b) Exponential fit to coarse grained density profile in dilute isotropic region. The gravitational length was obtained by fitting a straight line to the log plot shown in the inset. The body of the figure shows the fit against the coarse grained density profile. The fit yields $l_g = 0.9 \pm 0.1\,\mu m$.

by assuming the core rod has the shape of a cylinder with one hemispherical cap and a density of $1.90\,g\,cm^{-3}$ and the Stöber shells grow the rod to a spherocylindrical shape with volume given by Equation 2.12 with density $1.99\,g\,cm^{-3}$ [32]. This calculation yields a value of $0.53\,\mu m$, compared to $0.9\pm0.1\,\mu m$ calculated from the tail of the density profile.

There are several factors which may contribute to this discrepancy. The first is the polydispersity, or rather the size segregation through the sediment. As many large particles are observed to be at the glass slide, the particles higher in the sediment must have mean sizes lower than the global mean of the system. The gravitational length calculated from the sedimentation profile is found to be almost twice that calculated based on the mean hard particle size. The effect of size segregation has been reported in literature [56] where it was found that a (diameter) polydispersity of 4.6% in sedimenting colloidal spheres resulted in an 11% higher measured gravitational length. The polydispersity was concluded to fully account for the apparent extension of the sedimentation profile of well screened particles (as with the rod-like silica particles studied here) so the very large increase in l_g is not in agreement with this previous research. However, the polydispersity in this rod system is somewhat higher than 4.6% so it is conceivable that the effect of size segregation is greater in this system.

A similar discrepancy of about a factor of two was found earlier by Piazza et al. [57]. In this case the extension of the sedimentation profile was attributed to a macroscopic electric field set up by the concentration of charged particles at the bottom of the sediment which acts to repulse the higher particles against gravity. It was shown that this discrepancy was a function of the sediment height with the calculated values approximately recovered for low sediments. Due to the comparatively low sediments in this investigation, it is concluded that this electric field effect is not the principal factor. However, if the particle size segregation leaves all the small particles at the top of the sediment, it is possible that they may be affected even by a very weak electric field set up in the low sediment.

The Phase Transition

The phase transition from crystal/columnar/smectic to isotropic not only has a density drop associated with it but also a decrease in the degree of order in the system. This may be quantified
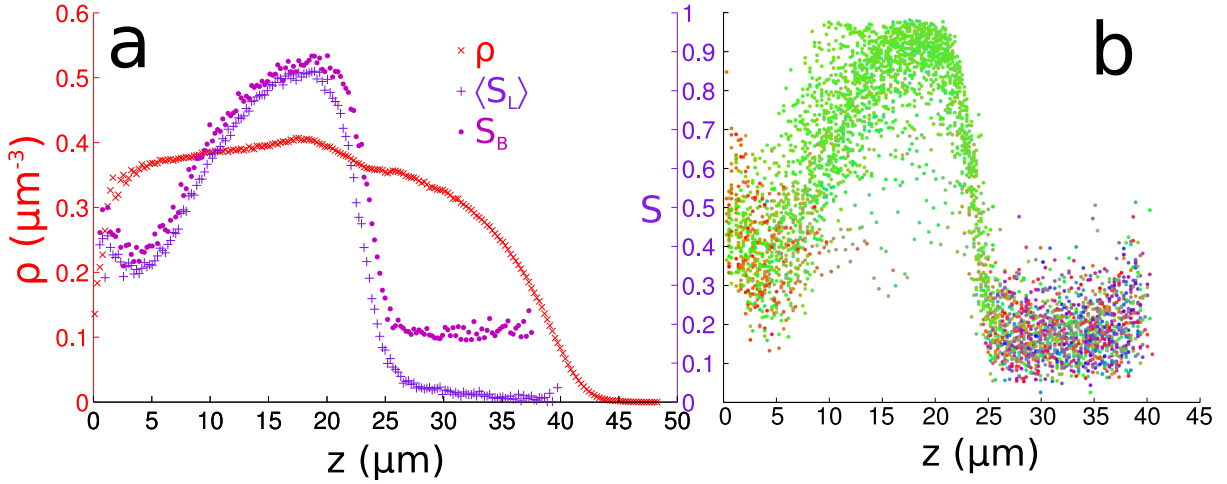
Figure 4.15.: (a) Averaged Local (S_L) and bin averaged (S_B) nematic order parameters plotted on the same horizontal axis as the number density. (b) Nematic order parameter values with the colour showing the direction of the nematic director according to their alignment with the three axes as in Figure 4.10a. The colours indicate direction, not level of order, not to be confused with Figure 4.13. These are the values which are averaged over the 24 volumes to give the S_B values in (a). The central axis is shared between (a) and (b).

by examining the nematic order parameters at different points in the sediment. Average values are plotted in Figure 4.15a.

Both order parameters are seen to fall briefly at low z away from the orientational restriction imposed by the glass slide. The order parameters then rise to values typical for a smectic phase (≈ 0.9) as the domains become larger. The phase transition is clearly indicated in the cascade of both order parameters towards 0 which indicates the lack of average orientation in the isotropic phase. The reason that the bin averaged order parameter, S_B, does not reach 0 is due to the small numbers of particles in each bin after the phase transition. It is possible to use larger bins but this comes at the expense of resolution in the profile and for this data, it was not found to be possible to reach a large enough bin size such that each bin has at least 100 particles in it without blurring the transition. Figure 4.15b shows the same nematic order parameter without averaging over the 24 frames, with each point coloured to indicate the direction of the nematic director in the bin. After the transition, the rapid fluctuations and spread of values up to around 0.4 show that not enough particles are being taken into account but the multitude of colours in this region is indicative that the non 0 value is due to noise and that this is indeed the isotropic phase.

Figure 4.15a also shows the mean of the local order parameter, $\langle S_L \rangle$, in each bin, averaged over the 24 volumes. This parameter is less affected by the decreasing density and it is found that the values does decay to 0 after the sharp transition.

Figure 4.16 shows a zoomed in region of the nematic order parameter and density plots at the phase transition. Hyperbolic tangent (tanh) fits are shown which are used to determine the transition midpoints. There is a clear shift in the midpoints of the transition in density and in order parameter. This is denoted δ and has been reported for hard spherocylinders both in theory and in simulations, which predict values of $0.45\,\mathrm{L}_{cy}$ (DFT) [58] and $0.38\,\mathrm{L}_{cy}$ (simulations) [59] for the isotropic-nematic transition. In the present study, the shift was found to be slightly different depending on the order parameter used with the average of the local order parameter yielding a shift $\delta_{local} = 1.49 \pm 0.08\,\mu\mathrm{m} = 0.54 \pm 0.03\,\mathrm{L}_{cy}$ (assuming a perfect spherocylinder). The classic nematic order parameter yielded a higher value of $0.74\,\mathrm{L}_{cy}$ but the reliability of this value

37

is called into question by the undersampling in the isotropic phase discussed previously.

This phenomenon may intuitively be understood by considering a particle in the coexistence region. If the dense phase below it is (crudely) approximated by a hard wall then the particle's orientation is restricted to less than the unit sphere until it is half of its length away from the wall as the most upright orientations would cause the end of the rod to be inside the ordered phase. Naturally, there are more complicated dynamics at work at the interface and the shift is not exactly 0.5L. The magnitude of the shift found here is in qualitative agreement with the simulational and theoretical ones and it is important to note that these predictions were based on an isotropic-nematic interface and the interface discussed here involves a denser ordered phase than the nematic. This could account for the higher value obtained: the crystal-like phase is more like the hard wall in the preceding description whereas a nematic surface is less flat and so could accommodate particles of more varied orientations close to the wall.

The asymptotes of the tanh fits are used to estimate the densities at the top and bottom of the coexistence region. Using the mean rod size to estimate the volume of a single particle, this yields reduced volume fractions, ϕ/ϕ_{cp} (where ϕ_{cp} is the volume fraction at close packing based on a Smectic-B arrangement [21]) (for comparison to Figure 2.3), of 0.459 and 0.399 for the upper and lower bounds of the coexistence region. These values are rather lower than those predicted in simulations at the same aspect ratio $\phi/\phi_{cp} = 0.532$ and $\sim$0.69 at L_{cy}/D=4.4 (using the assumption that the nematic and smectic-A phases are hidden within the coexistence region) [25].

The reason for this disparity is the same one that accounts for the lack of nematic and smectic-A phases: the particles are not as ideally hard as those used in simulations but are negatively charged and hence have an electrical double layer around them. This means that they cannot approach close enough to touch and therefore lower densities are observed. Following the work of Kuijk et al. [8], an attempt was made to take the double layer into account by estimating its size and then modifying the size of the rod with the increase in effective dimensions due to the double layer.

The extent of the double layer was estimated by taking the average separation of the particles close to the bottom of the sediment (where it is assumed that the particles are under high enough pressure as to be at their distance of closest approach). This yielded an effective diameter of 860 nm, 229 nm greater than the hard one measured from TEM images. The correction was added to both the diameter and the length of the particle and its volume recalculated. This reduced the aspect ratio by 1.2 and increased the coexistence densities to 0.902 and 0.794, which are both much higher than the values predicted by simulations for transitions at this aspect ratio ($L_{cy}^{eff}/D^{eff} = 3.2$).

The largest particles are found at the bottom of the sediment, therefore it is likely that this method of estimating the double layer results in some overestimation. Another method of estimating the double layer is to use Equation 2.1 and Walden's rule which may be used to estimate the limiting equivalent conductance and hence the ionic strength of the solvent (Section 3.3 [60]).

Along with the measured conductivity of 0.137 μScm^{-1}, and Equation 2.1, the Debye length is estimated to be rather small at 22.2 nm, with a corresponding estimated effective diameter of 675 nm. The coexistence densities calculated with these effective dimensions (relative to close packing) are 0.532 and 0.462, which when compared to Figure 2.3 at the new effective aspect ratio, $L_{cy} = 4.07$ are found to be close to the simulational predictions for the boundaries for the nematic phase, but still somewhat low given that the observed transition involves a crystal-like phase.

It is therefore concluded that the true effective dimensions including the double layer lie in between the hard and soft limits which are outlined here. The three pairs of coexistence densities are shown in Figure 4.17 at their effective aspect ratios. Good agreement with simulations is found in the density change across the isotropic-smectic coexistence region with the large double
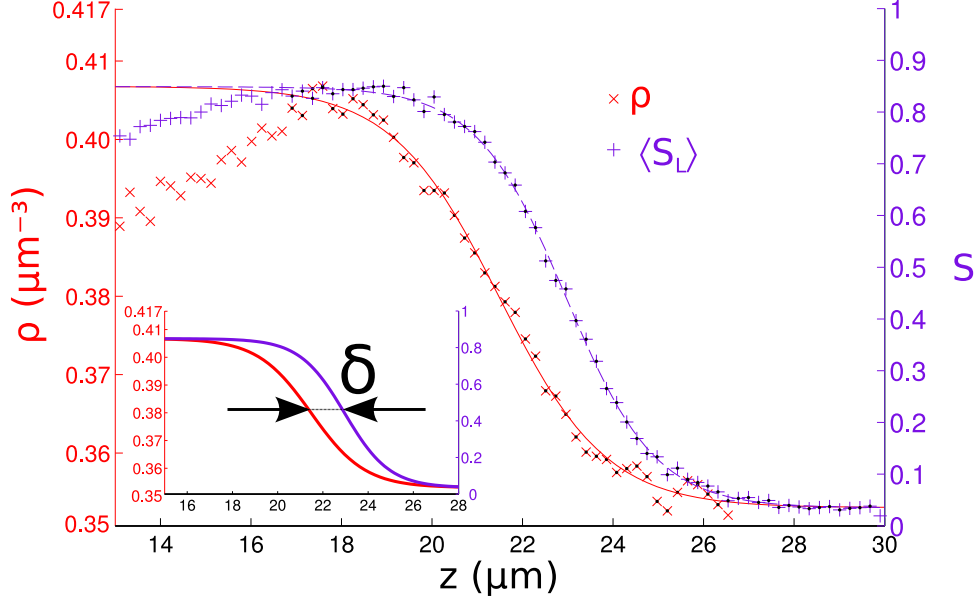
Figure 4.16.: Hyperbolic tangent fits to the coarse grained density (ρ) and mean local nematic order parameter ($\langle S_L \rangle$) profiles across the phase transition.

layer correction. The decrease in $\phi/\phi_{cp}(= \rho^*$ in Figure 4.17) with $L_{cy}^{eff} = 3.2$ was found to be 13% compared to 16% in simulations of particles with $L_{cy}/D = 3.4$ and 14% for particles with $L_{cy}/D = 3.0$ [25].

4.5.3. The Equation of State

As discussed in Section 2.2, once the density profile is known, the osmotic equation of state may be obtained by integration to obtain the pressure distribution followed by elimination of z between the profiles. Due to the size segregation in the sediment, integration of the complete density profile shows the density decreasing as the pressure increases close to the bottom. As this is unphysical and known to be due to the particle sizes, only the region above the maximum in density is used to calculate the equation of state (Figure 4.18).

The different phase regions are marked on the equation of state in Figure 4.18. For a truly first order transition, the coexistence region would manifest itself as a horizontal discontinuity. This is not observed in the equation of state of this system. However, the inflection point is observed at the isotropic side of the transition. The necessity of only including a small region of the crystal-like phase in the equation of state means that the inflection point at the denser side of the coexistence is unclear. The pressure at the onset of the transition was found to be around $\Pi V_p/kT = 18$ which is approximately twice as high as that predicted by computer simulations [25]. This is a difficult comparison to make as the measured result is not only affected by the effective particle dimensions discussed in Section 4.5.2 but also by the compressibility of the double layer, which would likely affect the pressure required for a phase transition.

As the effective dimensions of the particles seem to have pushed the aspect ratio to the region of the phase diagram where only the crystal-like and isotropic phases are predicted, it is surprising that the large coexistence region does not show a clear discontinuity in the plot of the equation of state. It is known that interfaces are not in general planar and in fact undergo fluctuations in the form of capillary waves [59]. It could be that averaging the density profile over an area larger than the wavelength of these fluctuations causes blurring of the interfacial discontinuity. It is possible to average over a smaller area, but this causes the profile to become very noisy which also makes the interfacial position unclear.
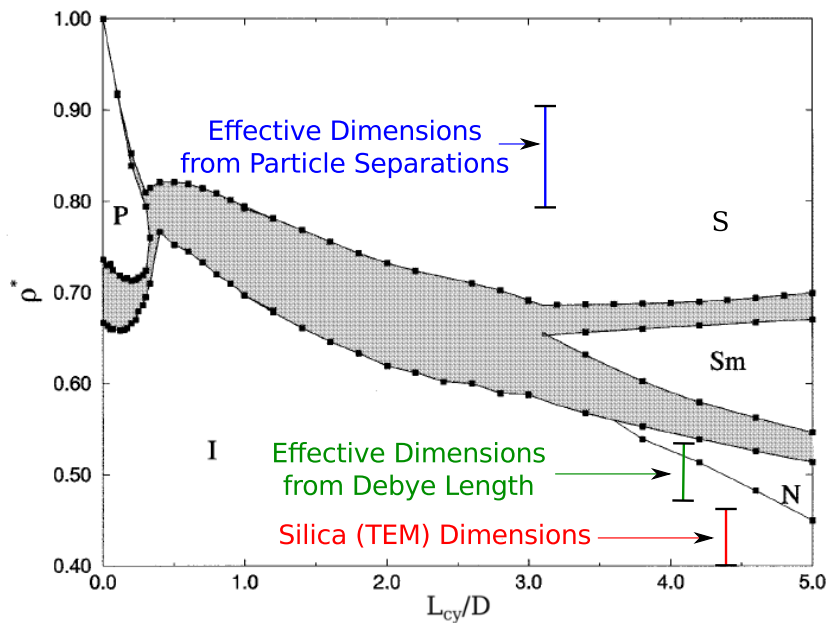
Figure 4.17.: Phase diagram predicted by computer simulations [25] with experimental coexistence densities marked.
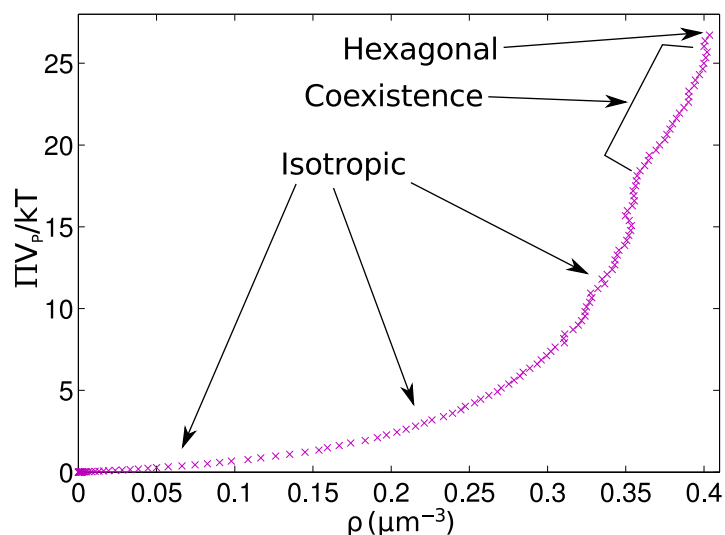

Figure 4.18.: Equation of state for rod-shaped particles with $L/D = 5.4$. The pressures are scaled with the particle volume divided by the thermal energy.
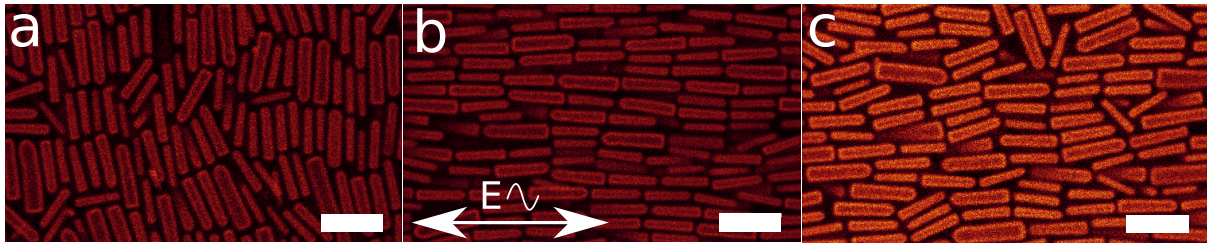
Figure 4.19.: Confocal images of rods at the bottom of the sediment (lying on the glass slide). (a) Before electric field application. The greater alignment in this image than, for example, Figure 4.11c is that the two wires used to apply the field act as walls, inducing this orientation. (b) Field on. (c) 8 minutes after field turned off. All scale bars are 4 μm. The concentrated sediment on top of these particles extended for approximately 30 μm at this time.

4.6. External Alignment of Particles with an Electric Field

In order to find out whether the same behaviour would be observed when starting from a fully aligned arrangement, an electric field was used to align the particles in the sediment and then allowing them to equilibrate. Figure 4.19 shows images of the particles at the glass slide before, during and after the application of the electric field. Figure 4.19b clearly shows that the particles were realigned by the field , despite their initial configuration approximately perpendicular to it. When the field was turned off, the particles retained the average orientation that had been given to them but after only 8 minutes (Figure 4.19c), the level of ordering was found to be comparable to that before the field application.

The system was then allowed to equilibrate for 59 days and re-examined (Figure 4.20). The similar appearance of Figures 4.19c and 4.20b shows that the particles relaxed to their preferred configuration only a few minutes after the field application. This preferred arrangement is very similar in terms of order to that observed before the external alignment of the particles.

The bottoms of Figures 4.20c,d show the large particles at the bottom of the sediment again disrupting the hexagonal ordering. Hexagonally ordered particles may be observed at around 10 μm in 4.20c and above this there is a large region where planes may be observed. Due to the limiting resolution of confocal microscopy being that in the z direction, when a close packed direction of the hexagonal lattice is vertically aligned as like this, the fluorescent signals of adjacent particles tend to overlap. This unfortunately excludes the possibility of single particle fitting of the full sediment in this case. From these images it is not clear whether or not these particles are hexagonally ordered, (but with a rotated orientation of the 'crystal' planes relative to the particles below) or in some other arrangement.

Figure 4.20d shows a view perpendicular to that of 4.20c such that most of the particles are viewed from the side. Interesting to note in this image is the formation of domains between the smectic layers which extend across a large z distance. These frequently have orientation perpendicular to the layers as in the right of Figure 4.20d and scattered across 4.20e. Figure 4.20(e) shows the long range smectic layering at a height of 20 μm, with the director corresponding to the direction of the electric field that was present nearly two months before.

From these observations it is concluded that artificial alignment of the particles during sedimentation increases the size of layered domains in the sediment, with the effect particularly noticeable low in the sediment. The region affected by the large local polydispersity is clear and the increase in domain size is much more rapid than in uninterrupted sediments. This would appear to show that in sediments unaffected by electric fields, the large particles not only disrupt the phase behaviour in the region at the bottom where they cause high local polydispersity but also in the region above them. The slow increase in domain size in natural sediments would seem to be a kinetic effect where the particles build on top of the polydisperse region
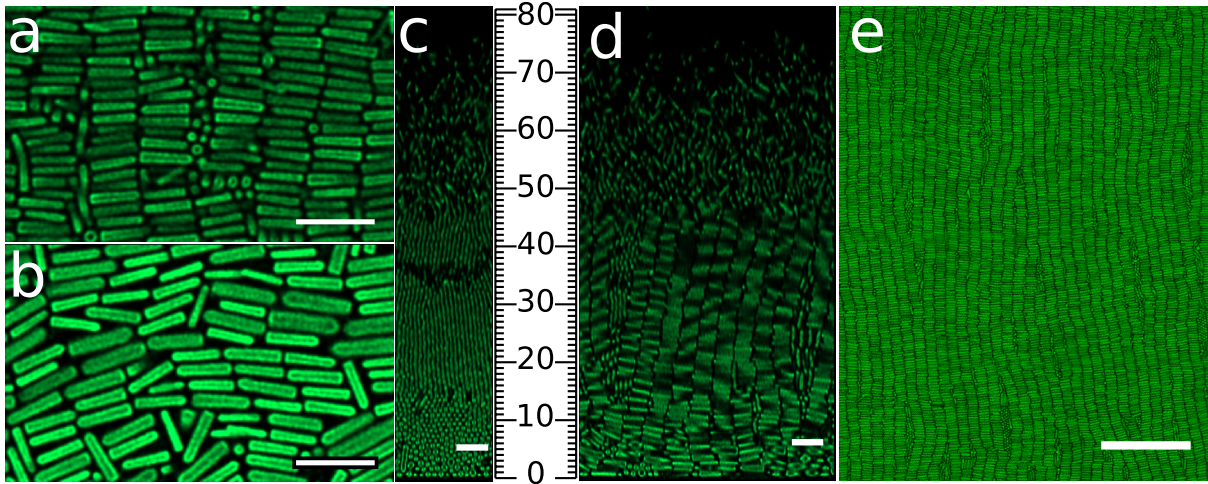
Figure 4.20.: 59 days after the field application. xy views shown at (a) 0 µm, (b) 10 µm and (e) 20 µm. (c) and (d) show different slices in the z direction against a micrometer scale. Scale bars are 5 µm (a-d) and 25 µm (e).

below, forming a disordered region. These then undergo some rearrangement but before they can form large domains they are trapped in small ones by the increasingly slow dynamics as particles build on top of them. This would explain the increase in domain size at higher height as each layer has successively less pressure applied to it and hence has more opportunity for rearrangement.

4.7. L/D=5.8 System: Preliminary Results

The system discussed in this section was set up by allowing the least polydisperse, highest aspect ratio particles to sediment from isotropic suspension in glycerol/water mixture with the salt concentration controlled with lithium chloride (see SGW in Table 3.1 and Appendix A). After 20 days, a volume of dimensions $35 \times 24 \times 50$ µm (voxel: $51 \times 51 \times 84$ nm) was imaged (Figure 4.21(a-c)) and the particle coordinates fitted (Figure 4.21d). As it cannot yet be confirmed if the sediment has reached equilibrium (and the few particles high above the sediment suggest that it has not), the results presented here are discussed as a first look at a promising system.

Figures 4.21b and c show that the particles at the glass slide were much less polydisperse than in the lower aspect ratio systems and that the particles formed a large domain columnar phase, with defects, from the very bottom. Figures 4.21a and 4.22a show that the smectic layering of the particles became more pronounced away from the slide but that the defect concentration remained similar. Where differently oriented domains were observed (not shown), they were found to extend up to the interface with the isotropic phase, not increasing their x-y extent with increasing z height as was observed in Section 4.4.2.

Figures 4.22b and c show that in some regions clear correlation between the hexagonal layers may be observed. The AAA stacked arrangement is once again assigned to a crystal slightly frustrated towards the columnar phase and the fact that AAA stacking may not be confirmed in all regions is taken to indicate that the very similar ABC crystal and smectic-B phases may also be present. This is similar in essence to the observations in Section 4.4.2 but in this case correlations may be found more frequently, presumably due to the decreased length polydispersity ($\sigma_L \approx 9\%$ compared to $\sigma_L \approx 12\%$ in the $L/D = 5.4$ system) and therefore level of frustration of the crystal.

Density and local order information are presented in Figure 4.23. The raw density profile shows rapid oscillations due to the well defined layering in z but the coarse profile reveals that
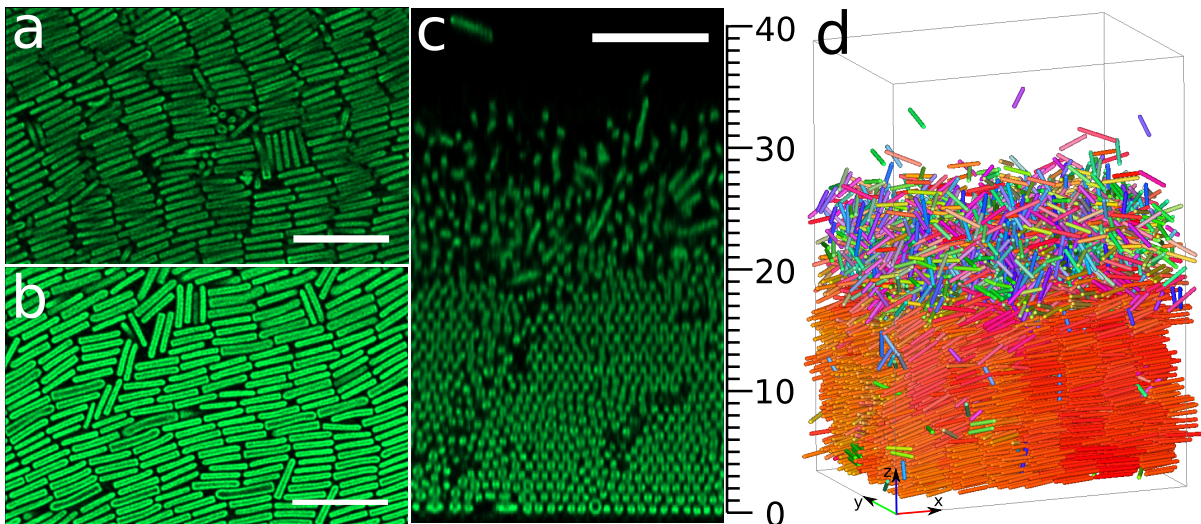
Figure 4.21.: L/D=5.8 system after 20 days of sedimentation. xy views shown at (a) 10 µm and (b) 0 µm. (c) shows a view in z against a scale of µm. A rendering of the 6587 particles after feature fitting is shown in (d). Scale bars are 10 µm.
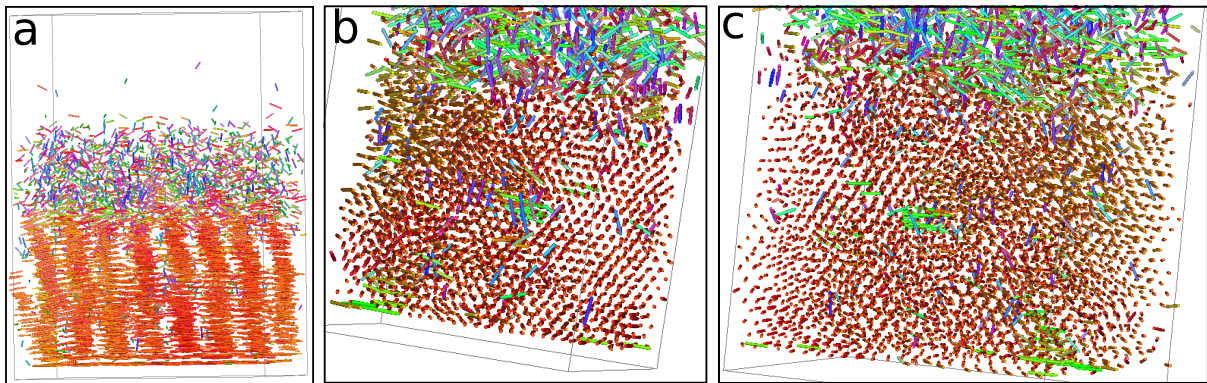

Figure 4.22.: Different views of the rendering with the particles made smaller for clarity. (a) Side view showing layering of particles. (b) View thorough 3 layers showing AAA stacking in centre-right of the image. (c) View though whole sediment showing 'crystal' planes in the left of the image. The stacking pattern is less discernible here.

there are enough large particles at the bottom to make the density appear lower there, but only slightly. Both nematic order parameters show a cascade at the transition to the isotropic phase and the density profile again shows a change in gradient, and not a true discontinuity. A small defect cluster is observed as a dip in the averaged order parameters and can be localised in the S_L scatter plot (Figure 4.23d). The dark blue points in this plot indicate particles surrounded by perpendicular ones, showing up interstitial particles and illustrating another advantage of this order parameter.

The Nematic Phase?

Figures 4.24(a-c) show images of the region just above the end of the hexagonally ordered region which appears to contain a very thin layer of the nematic phase between 19 and 22 µm. As the coexistence region between the columnar/smectic/crystalline region always exhibits some degree of ordering, the appearance of the nematic phase is difficult to confirm. However, in this sediment the alignment was noticed to last a little longer than in the shorter aspect ratio
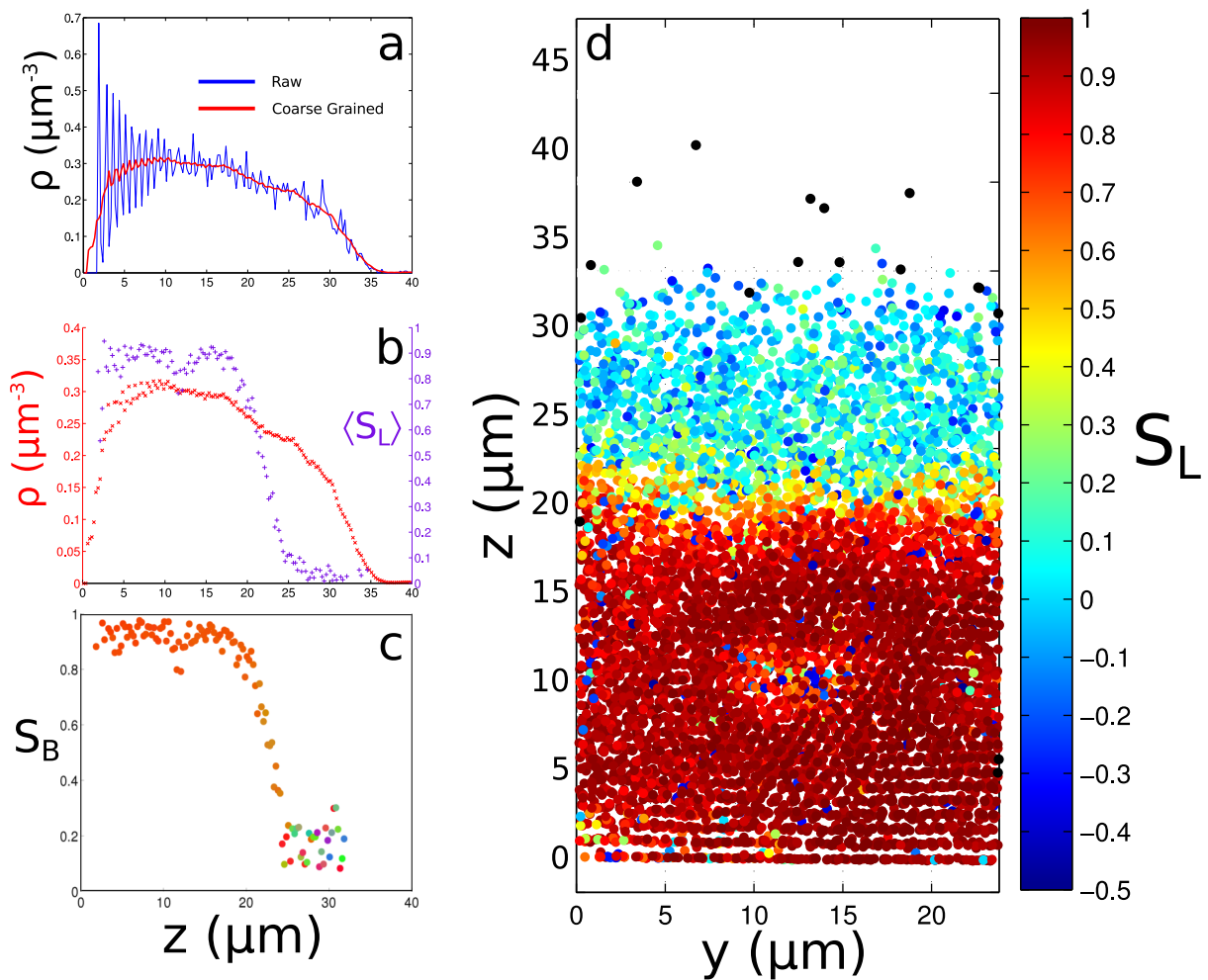
Figure 4.23.: Analysis of the particle coordinates. (a) Density profiles (b) Averaged local order parameter and the coarse grained density profile (c) Nematic order parameter with colouring indicating nematic director orientation in accordance with Figure 4.21d.

particles in previous sections.

Neither the density or nematic order parameter profiles show a second change in gradient in the right region that might indicate another phase transition. The local order scatter plot in Figure 4.24d does appear to show a larger (in z) region of yellow/orange after the smectic layering disappears than the corresponding figure for $L/D = 5.4$ particles (Figure 4.13c) . Also, the value of S_B is 0.52 at 21 µm which is a feasible value in a nematic phase. The colouring of the order parameter plot shown in Figure 4.23 may additionally support this nematic assignment. The colouring is indicative of the orientation as in Figure 4.21d and what it shows is that the average orientation in the coexistence region is not quite parallel to the director in the smectic layers below. The change from orange to a yellowish ochre shows that the director shifts slightly towards the y axis. This is in contrast to the $L/D = 5.4$ system in which the director in the coexistence region remains parallel to that in the smectic layers (Figure 4.15b).

This observation is not yet conclusive, but does give an early insight into the interesting behaviour of this system, which will be examined in more detail once it has fully equilibrated.
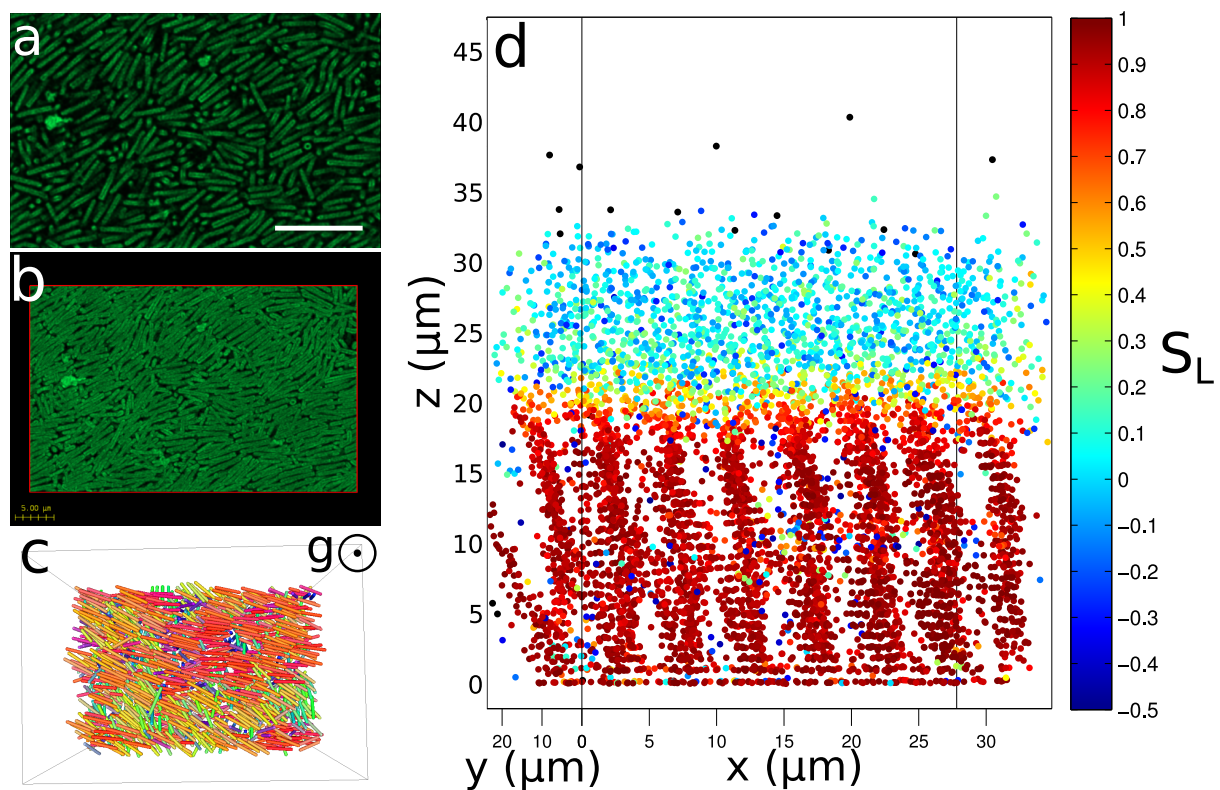

Figure 4.24.: Images of the region just above the end of the hexagonally ordered region, tentatively identified as the nematic phase. (a) xy view at 20 µm. Scale bar is 10 µm. (b) xy projection of the region approximately between 19 and 22 µm. (c) Rendering of the same region as in (b) with the particles above and below cut away. Gravity is in the same direction in (b) and (c) with both images looking upwards towards the isotropic.

5. Conclusions and Outlook

5.1. Conclusions

An experimental procedure for the study of sedimenting rod shaped silica colloids has been developed with a focus on 3D real space particle fitting. This has been used to investigate the behaviour of equilibrium sedimentation profiles of $L/D = 4.7$ and 5.4 particles with L the end-to-end length of the rod and D the diameter..

The polydispersity of the colloidal particles was found to have a great, and arguably dominating, effect on the phase behaviour. This is due to size segregation of the particles as they sediment, resulting in a high concentration of large particles close to the bottom. This caused a reduction of the particle ordering in this region, even when the particles were externally aligned with an electric field, although in this case the effect of the polydisperse particles was lessened. With the smaller and less polydisperse particles higher up, semi long range hexagonally ordered phases were observed with intriguing layering characteristics. Periodicity was observed along the director in these phases to varying degrees and in some regions AAA stacking was observed. Simulations on hard spherocylinders predict that the system would prefer to adopt the ABC crystalline arrangement were it not for the length polydispersity which means that the particles did not fit in their layers properly and the system was pushed slightly towards a columnar phase. It seems that this was enough to induce AAA crystalline stacking in some regions (as this is the only stacking pattern that makes sense for a columnar phase). The smectic-B phase is thought to be present also as many regions lacked interlayer correlation.

The nematic and smectic-A phases predicted by simulations at the aspect ratios used were not observed in the equilibrium sediments. This is thought to be due to charge effects which increase the effective particle dimensions with an electrical double layer, resulting in a significant decrease in the effective aspect ratio.

Density and nematic order parameter profiles were extracted along the full height of the sediment and the phase transition was examined. The double layer is thought to be partially responsible for the low coexistence densities measured in this research compared to simulations of hard spherocylinders. Attempts were made to estimate the size of the double layer to find out the effective dimensions. These corrections gave semi qualitative agreement with the simulated coexistence densities. The equation of state was found to be continuous across the phase transition, but its measurement was somewhat hampered by the polydispersity of the system disrupting the density profile data. The shift between the drop in density and order parameter profiles was found to be in close agreement with simulations and theory.

In a promising new system of $L/D = 5.8$ particles, a thin region of what appeared to be the nematic phase was observed above a highly ordered smectic/columnar/crystalline region. However, as this system has not yet fully equilibrated, judgement is reserved on the equilibrium phase behaviour until it has had more time for sedimentation and rearrangement and the reaching of a steady state may be verified.

5.2. Outlook

The higher aspect ration system presented in Section 4.7 shows promising behaviour which will be investigated in detail once it has equilibrated. It also has the advantage that the ionic strength is known so the Debye length may be accurately calculated.

5. Conclusions and Outlook

In future work it would be beneficial to know the ζ potential of the colloidal rod surface for a better understanding of the repulsive interactions. This measurement may present more experimental challenges than the same one on spherical particles due to their anisotropy.

Of course it is of interest to look at less polydisperse particles with even higher aspect ratios and this may be achieved by building on the results of this research. Single particle fitting applied to cm scale sediments observed from the side may also provide more insight into the equilibrium behaviour of the system.

In this investigation, the particle length fitting was not focussed on as it was already difficult to extract the correct centre of mass and orientation. With more separated particles, it would be of interest to gain an accurate estimate of the particle length distribution at different heights. This would allow detailed insight into the size segregation and possible fractionation effects on the liquid crystal phase behaviour, as well as providing a way of obtaining more accurate volume fraction estimates.

A. Control of the Ionic Strength in Glycerol/Water Mixtures

For accurate estimates of the Debye screening length, it is necessary to know the ionic strength of the solvent mixture. When it is controlled by trace ions present in the solvent as supplied, the ionic strength is not known. By adding a strong electrolytic salt to the mixture, the effect of the trace ions may be masked such that the ionic strength is determined by the known salt concentration. In order to achieve this in glycerol/water mixtures, lithium chloride salt may be used.
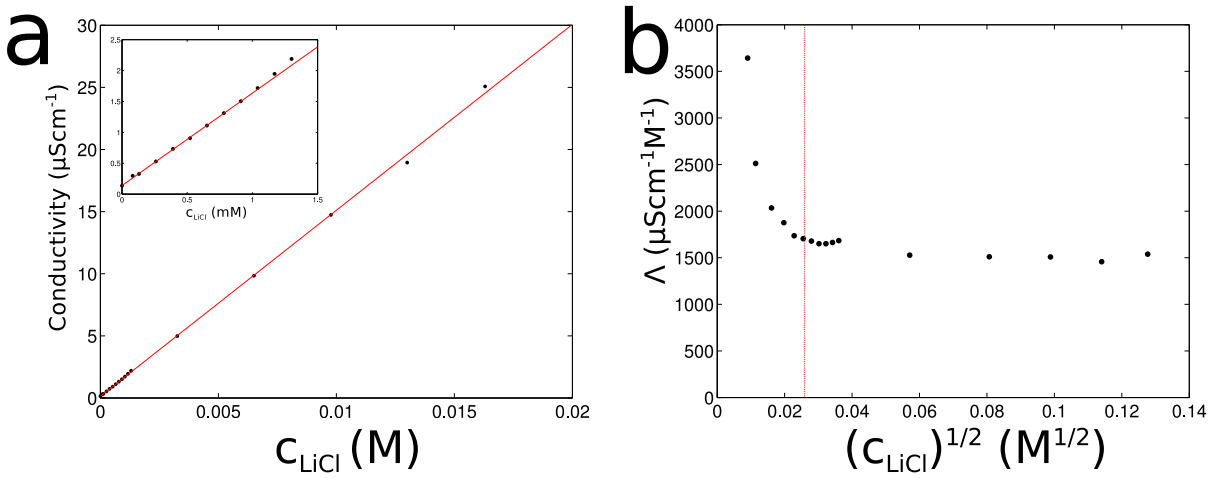

Figure A.1.: Conductivity Measurements. (a) Linear relationship between added salt concentration and measured conductivity. Inset shows region at low salt concentration against the same vertical scale. (b) Molar conductivity as a function of the square root of the concentration. Red dotted line shows point at which the effect of the trace ions on the ionic strength of the mixture is masked by the added salt. This corresponds to 5.5×10^{-4} M or 4.5×10^{-4} molkg^{-1}.

Figure A.1 shows the results of conductivity measurements in glycerol/water (85:15 wt.) mixtures at a series of salt concentrations. Figure A.1a clearly shows the linear dependence of the conductivity on the salt concentration, which is characteristic of strong electrolytic behaviour. Figure A.1b shows the conductance per mole of added salt, Λ, against the square root of the concentration (the square root is used with Kohlrausch's empirical law in mind [43]):

$$\Lambda = \Lambda^0 - A\sqrt{c_{salt}} \tag{A.1}$$

Here Λ^0 is the limiting equivalent molar conductance at infinite dilution and A is an electrolyte specific constant. The plot shows Λ very high initially due to the fact that here the trace ions (whose concentration is not included in the division) are still contributing to the measured conductivity. For a strong electrolyte Equation A.1 applies and Λ is expected to decrease slightly with the root of the salt concentration but here it was observed to remain constant, after the effect of the trace ions had been masked. This could be due to the decrease being too subtle for this measurement or to the low salt concentrations tested. The reason for the slight increase in Λ just below $c^{1/2} = 0.04 M^{1/2}$ is not known.

A. Control of the Ionic Strength in Glycerol/Water Mixtures

Based on the levelling of Λ in Figure A.1b, the trace ion contribution to the ionic strength is thought to be sufficiently masked at lithium chloride concentration of $0.023\,\text{M}^{1/2}$ which is equivalent to $5.5\times10^{-4}\,\text{M}$. Experimentally, it is often more convenient to use the equivalent molal concentration of $4.5\times10^{-4}\,\text{molkg}^{-1}$. At this ionic strength, the Debye length is calculated to be $10.3\,\text{nm}$ which is approximately half of the estimated value in the mixture when the ionic strength is controlled by the trace ions ($22.2\,\text{nm}$).

B. Electric Field Cell

A method to build a cell with which to apply an electric field to a sedimenting system of colloids is described here as a supplement to Section 3.2.2. A schematic of the cell is shown in Figure B.2.

1. Clamp a rectangular cover-glass together with a normal microscope slide close to the table.

2. Cut a length of thermocouple wire and clamp one end in a pair of heavy pliers and place them on the table to one side of the slide.

3. Wind the free end of the wire around the length of the slide to make two rails along the centre (looks like a stretched 'z' shape with view through slide included, see Figure B.1).

4. Clamp the free end in similar pliers and place on the table at the opposite side to the other clamped end. The rails may then be adjusted by moving the pliers until they are parallel and very close together.

5. Once satisfied with their arrangement, tape the rails to the cover glass on either side of the middle. Some tightening and re-taping is possible if they do not hold their tension.

6. Cut the wires such that two long ends are left (one of them is made from the diagonal section of the 'z', the dotted part in Figure B.1) and the other ends are short, separate and sealed in place (on the right in Figure B.2).

7. Seal the bottom of the cell.
   - For a glue sealed cell, glue the pipette end down over the rails and proceed then feed the column through a slide with a hole in it and glue in place. Remember to bring the thermocouple wires up to the top side (not shown in figure).
   - For a wax sealed cell, glue the cover-glass/wire rails over the hole in the slide first. Then apply a thin rim of candle wax to the pipette end and clamp it with the wax upwards. Place the slide/wire/cover-glass construction such that it balances on top of the clamped pipette end, with the wax in contact with the cover-glass. Heat the
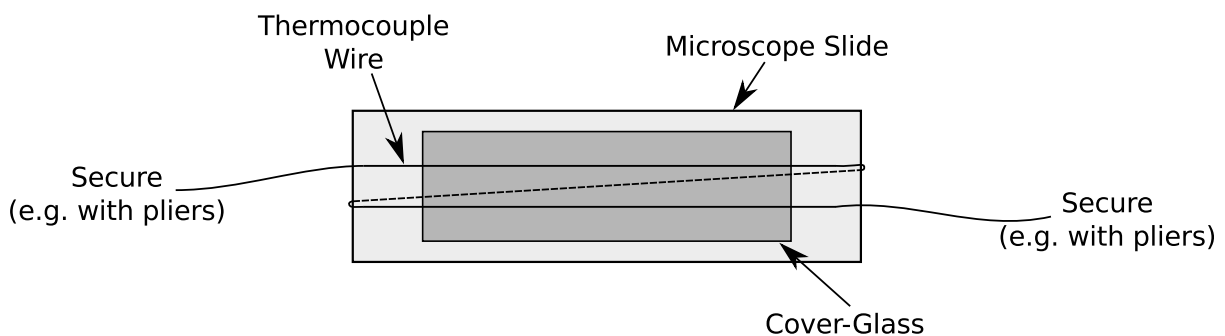

Figure B.1.: Illustration of step 3 in the cell building process. The distance between the rails is exaggerated for clarity. The glass slide shown here does not have a hole in it and is simple used for holding the cover-glass in place during the laying of the rails. It is discarded once the rails are taped to the cover-glass.
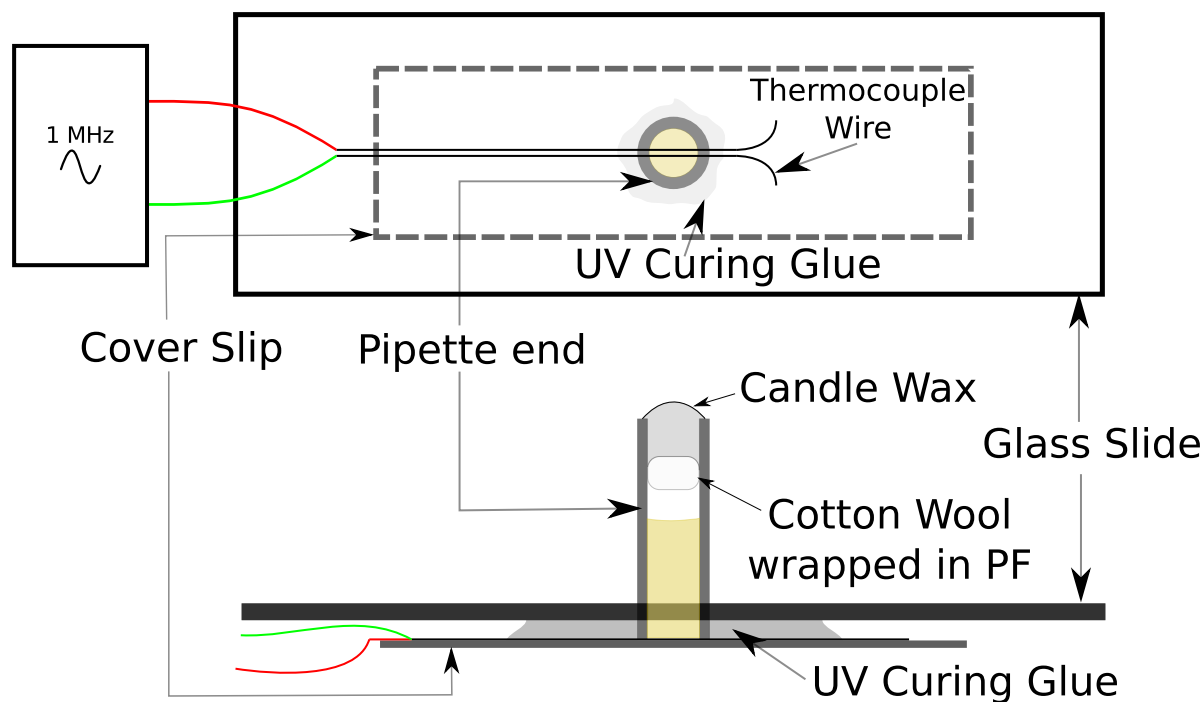
Figure B.2.: Simplified schematic of the electric field cell. In practice, the long ends of the thermocouple wire must be brought up around the sides of the microscope slide to the top before attaching to insulated cable. Without doing this, the cell may not sit horizontally on a conventional microscope stage. PF refers to Parafilm.

pipette end lightly at the free end until the wax melts, sealing the bottom of the cell. Add UV glue around the bottom of the column for structural support.

8. Tape the wires to topside of cell (not shown), separately! Ensure the wires coming up the sides are well insulated.

9. Attach the thermocouple wires to two different colours of insulated cable (ensure these are long enough to reach down from the microscope stage) and tape down the connections.

10. The insulated wires may be held in place with additional UV glue to prevent the connections breaking if they are tugged accidentally.

Bibliography

[1] B. Vincent, "Introduction to colloidal dispersions," in *Colloid Science*, Blackwell Publishing, 2005.

[2] A. D. McNaught and A. Wilkinson, eds., *IUPAC. Compendium of Chemical Terminology*. Blackwell Scientific Publications, 1997.

[3] D. Frenkel and B. Smit, *Understanding Molecular Simulation*. Academic Press (Elsevier), 1996.

[4] T. F. Tadros, "Colloids in Paints," in *Colloids in Paints: Colloids and Interface Science, Volume 6*, Wiley-VCH, 2010.

[5] L. Juszczak, Z. Oczady, and D. Gakowska, "Effect of Modified Starches on Rheological Properties of Ketchup," *Food and Bioprocess Technology*, vol. 6, pp. 1251–60, 2012.

[6] S. A. Rinne, F. García-Santamaría, and P. V. Braun, "Embedded cavities and waveguides in three-dimensional silicon photonic crystals," *Nature Photonics*, vol. 2, pp. 52–6, 2007.

[7] J. Crocker and D. Grier, "Methods of digital video microscopy for colloidal studies," *Journal of Colloid and Interface Science*, vol. 179, pp. 298–310, 1996.

[8] A. Kuijk, D. V. Byelov, A. V. Petukhov, A. van Blaaderen, and A. Imhof, "Phase behavior of colloidal silica rods," *Faraday Discussions*, vol. 159, pp. 181–99, 2012.

[9] T. H. Besseling, M. Hermes, A. Kuijk, B. de Nijs, T.-S. Deng, M. Dijkstra, A. Imhof, and A. van Blaaderen, "Determination of the positions and orientations of concentrated rod-like colloids from 3D microscopy data." arXiv: 1406.4985, 2014.

[10] A. van Blaaderen, *Colloidal Silica: Fundamentals and Applications*, ch. 18, pp. 233–5. CRC Press, 2005.

[11] J. Riley, "Charge in Collidal Systems," in *Colloid Science*, Blackwell Publishing, 2005.

[12] T. F. Tadros, "General principles of colloid stability and the role of surface forces," in *Colloid Stability*, Wiley-VCH, 2007.

[13] J. Eastman, "Colloid Stability," in *Colloid Science*, Blackwell Publishing, 2005.

[14] J. Israelachvili, *Intermolecular and surface forces*. Elsevier, 3rd ed., 1985.

[15] R. Piazza, "Settled and unsettled issues in particle settling.," *Reports on Progress in Physics*, vol. 77, p. 056602, 2014.

[16] T. Biben, J. Hansen, and J. Barrat, "Density profiles of concentrated colloidal suspensions in sedimentation equilibrium," *Journal of Chemical Physics*, vol. 98, pp. 7330–44, 1993.

[17] T. Svedberg, K. Pedersen, and J. Bauer, *The Ultracentrifuge*. Oxford University Press, 1940.

[18] S. Broersma, "Rotational Diffusion Constant of a Cylindrical Particle," *Journal of Chemical Physics*, vol. 32, pp. 1626–31, 1960.

[19] S. Broersma, "Viscous Force Constant for a Closed Cylinder," *Journal of Chemical Physics*, vol. 32, pp. 1632–5, 1960.

[20] M. M. Tirado, C. L. Martinez, and J. G. de la Torre, "Comparison of theories for the translational and rotational diffusion coefficients of rod-like macromolecules. Application to short DNA fragments," *Journal of Chemical Physics*, vol. 81, pp. 2047–52, 1984.

[21] A. Kuijk, *Fluorescent colloidal silica rods-synthesis and phase behavior*. PhD thesis, Utrecht University, 2012.

[22] L. Onsager, "The effects of shape on the interaction of colloidal particles," *Annals New York Academy of Sciences*, vol. 51, pp. 627–59, 1949.

[23] A. Stroobants, H. Lekkerkerker, and D. Frenkel, "Evidence for smectic order in a fluid of hard parallel spherocylinders," *Physical Review Letters*, vol. 57, pp. 1452–5, 1986.

[24] D. Frenkel, "Onsager's spherocylinders revisited," *The Journal of Physical Chemistry*, vol. 91, pp. 4912–6, 1987.

[25] P. Bolhuis and D. Frenkel, "Tracing the phase boundaries of hard spherocylinders," *Journal of Chemical Physics*, vol. 106, pp. 666–87, 1997.

[26] A. Kuijk, A. van Blaaderen, and A. Imhof, "Synthesis of monodisperse, rodlike silica colloids with tunable aspect ratio.," *Journal of the American Chemical Society*, vol. 133, pp. 2346–9, 2011.

[27] W. Stöber, A. Fink, and E. Bohn, "Controlled growth of monodisperse silica spheres in the micron size range," *Journal of Colloid and Interface Science*, vol. 69, pp. 62–9, 1968.

[28] A. Van Blaaderen, J. Van Geest, and A. Vrij, "Monodisperse colloidal silica spheres from tetraalkoxysilanes: Particle formation and growth mechanism," *Journal of Colloid and Interface Science*, vol. 154, pp. 481–501, 1992.

[29] S. Inoué, "Foundations of confocal scanned imaging in light microscopy," in *Handbook Of Biological Confocal Microscopy*, Springer, 2006.

[30] M. C. Jenkins and S. U. Egelhaaf, "Confocal microscopy of colloidal particles: Towards reliable, optimum coordinates," *Advances in Colloid and Interface Science*, vol. 136, pp. 65–92, 2008.

[31] V. Prasad, D. Semwogerere, and E. R. Weeks, "Confocal microscopy of colloids," *Journal of Physics: Condensed Matter*, vol. 19, p. 113102, 2007.

[32] A. Kuijk, A. Imhof, M. H. W. Verkuijlen, T. H. Besseling, E. R. H. van Eck, and A. van Blaaderen, "Colloidal Silica Rods: Material Properties and Fluorescent Labeling," *Particle and Particle Systems Characterisation*, vol. 31, pp. 706–13, 2014.

[33] M. van der Linden, "Real-space structure of colloidal hard-sphere glasses in experiments and simulations," Master's thesis, Utrecht University, 2008.

[34] M. Schwertner, M. J. Booth, and T. Wilson, "Simple optimization procedure for objective lens correction collar setting.," *Journal of Microscopy*, vol. 217, pp. 184–7, 2005.

[35] I. Malitson, "Interspecimen comparison of the refractive index of fused silica," *Journal of the Optical Society of America*, vol. 55, pp. 1205–9, 1965.

[36] T. H. Besseling, J. Jose, and A. van Blaaderen, "Methods to calibrate and scale axial distances in confocal microscopy as a function of refractive index." arXiv: 1404.3952, 2014.

[37] M. Cannell, A. McMorland, and C. Soeller, "Image enhancement by deconvolution," in *Handbook of Biological Confocal Microscopy*, pp. 488–500, Springer, 2006.

[38] H. T. M. van der Voort and K. C. Strasters, "Restoration of confocal images for quantitative image analysis," *Journal of Microscopy*, vol. 178, pp. 165–81, 1995.

[39] S. Hell, G. Reiner, C. Cremer, and E. H. K. Stelzer, "Aberrations in confocal fluorescence microscopy induced by mismatches in refractive index," *Journal of Microscopy*, vol. 169, pp. 391–405, 1993.

[40] M. Allen and G. Evans, "Hard convex body fluids," *Advances in Chemical Physics*, vol. 86, pp. 1–166, 1993.

[41] A. Cuetos and M. Dijkstra, "Kinetic pathways for the isotropic-nematic phase transition in a system of colloidal hard rods: A simulation study," *Physical Review Letters*, vol. 98, p. 095701, 2007.

[42] G. Janz and S. Danyluk, "Conductances of Hydrogen Halides in Anhydrous Polar Organic Solvents," *Chemical Reviews*, vol. 60, pp. 209–34, 1960.

[43] M. Leunissen, *Manipulating colloids with charges and electric fields*. PhD thesis, Utrecht University, 2007.

[44] J. Segur and H. Oberstar, "Viscosity of glycerol and its aqueous solutions," *Industrial and Engineering Chemistry*, vol. 43, pp. 5–8, 1951.

[45] P. Datskos and J. Sharma, "Synthesis of segmented silica rods by regulation of the growth temperature.," *Angewandte Chemie International Edition*, vol. 53, pp. 451–4, Jan. 2013.

[46] N. Martini, J. Bewersdorf, and S. W. Hell, "A new high-aperture glycerol immersion objective lens and its application to 3D-fluorescence microscopy," *Journal of Microscopy*, vol. 206, pp. 146–51, 2002.

[47] R. LeBel and D. Goring, "Density, Viscosity, Refractive Index, and Hygroscopicity of Mixtures of Water and Dimethyl Sulfoxide.," *Journal of Chemical Engineering Data*, vol. 7, pp. 100–101, 1962.

[48] H. El-Kashef, "The necessary requirements imposed on polar dielectric laser dye solvents," *Physica B*, vol. 279, pp. 295–301, 2000.

[49] J. Rheims, J. Köser, and T. Wriedt, "Refractive-index measurements in the near-IR using an Abbe refractometer," *Measurement Science and Technology*, vol. 8, pp. 601–5, 1997.

[50] D. El Masri, T. Vissers, S. Badaire, J. C. P. Stiefelhagen, H. R. Vutukuri, P. Helfferich, T. H. Zhang, W. K. Kegel, A. Imhof, and A. van Blaaderen, "A qualitative confocal microscopy study on a range of colloidal processes by simulating microgravity conditions through slow rotations," *Soft Matter*, vol. 8, pp. 6979–90, 2012.

[51] Z. Dogic, a. P. Philipse, S. Fraden, and J. K. G. Dhont, "Concentration-dependent sedimentation of colloidal rods," *Journal of Chemical Physics*, vol. 113, pp. 8368–80, 2000.

[52] A. Wysocki, C. P. Royall, R. G. Winkler, G. Gompper, H. Tanaka, A. van Blaaderen, and H. Löwen, "Direct observation of hydrodynamic instabilities in a driven non-uniform colloidal dispersion," *Soft Matter*, vol. 5, pp. 1340–4, 2009.

[53] G. Vroege, D. Thies-Weesie, a.V. Petukhov, B. Lemaire, and P. Davidson, "Smectic Liquid-Crystalline Order in Suspensions of Highly Polydisperse Goethite Nanorods," *Advanced Materials*, vol. 18, pp. 2565–8, 2006.

[54] E. van den Pol, D. M. E. Thies-Weesie, a. V. Petukhov, G. J. Vroege, and K. Kvashnina, "Influence of polydispersity on the phase behavior of colloidal goethite.," *Journal of Chemical Physics*, vol. 129, p. 164715, 2008.

[55] M. A. Bates and D. Frenkel, "Influence of polydispersity on the phase behavior of colloidal liquid crystals: A Monte Carlo simulation study," *Journal of Chemical Physics*, vol. 109, pp. 6193–99, 1998.

[56] C. P. Royall, R. van Roij, and A. van Blaaderen, "Extended sedimentation profiles in charged colloids: the gravitational length, entropy, and electrostatics," *Journal of Physics: Condensed Matter*, vol. 17, pp. 2315–26, 2005.

[57] R. Piazza, T. Bellini, and V. Degiorgio, "Equilibrium sedimentation profiles of screened charged colloids: A test of the hard-sphere equation of state," *Physical Review Letters*, vol. 71, pp. 4267–70, 1993.

[58] K. Shundyak, *Interfacial phenomena in hard-rod fluids.* PhD thesis, Utrecht University, 2004.

[59] S. Wolfsheimer, C. Tanase, K. Shundyak, R. van Roij, and T. Schilling, "Isotropic-nematic interface in suspensions of hard rods: Mean-field properties and capillary waves," *Physical Review E*, vol. 73, p. 061703, 2006.

[60] C. P. Royall, M. E. Leunissen, and A. V. Blaaderen, "A new colloidal model system to study long-range interactions quantitatively in real space," *Journal of Physics: Condensed Matter*, vol. 15, pp. 3581–96, 2003.

Acknowledgements